Manuscript Click here to view linked References

Title

microRNA-132 restores adult hippocampal neurogenesis and memory deficits in Alzheimer's disease

Authors

Hannah Walgrave[1,2], Sriram Balusu[1,2], Sarah Snoeck[3], Elke Vanden Eynden[1,2], Katleen Craessaerts[1,2], Nicky Thrupp[1,2], Leen Wolfs[1,2], Katrien Horré[1,2], Yannick Fourne[1,2], Alicja Ronisz[2,4], Edina Silajdžić[5], Amber Penning[3], Giorgia Tosoni[3], Zsuzsanna Callaerts-Vegh[2, 6], Rudi D'Hooge[2, 6], Dietmar Rudolf Thal[2,4], Henrik Zetterberg[7,8,9,10], Sandrine Thuret[5], Mark Fiers[1,2], Carlo Sala Frigerio[10], Bart De Strooper[1,2,10*], Evgenia Salta[3*]

[1] VIB Center for Brain & Disease Research, 3000, Leuven, Belgium

[2] KU Leuven, Leuven Brain Institute, 3000, Leuven, Belgium

[3]Laboratory of Neurogenesis and Neurodegeneration, Netherlands Institute for Neuroscience, 1105BA, Amsterdam, The Netherlands

[4]Laboratory for Neuropathology, KU Leuven, and Department of Pathology, UZ Leuven, 3000, Leuven, Belgium

[5] Institute of Psychiatry, Psychology & Neuroscience, King's College London, SE59RX, London, UK

[6] Laboratory for Biological Psychology, KU Leuven, 3000, Leuven, Belgium

[7] Clinical Neurochemistry Laboratory, Sahlgrenska University Hospital, S-431 80, Mölndal, Sweden

[8] Department of Neurodegenerative Disease, UCL Institute of Neurology, WC1N 3BG, London, UK

[9] Institute of Neuroscience and Physiology, Department of Psychiatry and Neurochemistry, the Sahlgrenska Academy at the University of Gothenburg, S-431 80 Mölndal, Sweden

[10] UK-Dementia Research Institute at UCL, WC1E 6BT, London, UK

* Corresponding authors

Correspondence

e.salta@nin.knaw.nl

b.strooper@ukdri.ucl.ac.uk

Lead contact

e.salta@nin.knaw.nl

Summary

Adult hippocampal neurogenesis (AHN) is functionally linked to mnemonic and cognitive plasticity in humans and rodents. In Alzheimer's disease (AD), the process of generating new neurons at the hippocampal neurogenic niche is impeded, yet the mechanisms involved are unknown. Here we identify miR-132, one of the most consistently downregulated microRNAs in AD, as a potent regulator of AHN, exerting cell-autonomous pro-neurogenic effects in the adult neurogenic niche. Using distinct AD mouse models, cultured human primary and established neural stem cells, and human patient material, we demonstrate that AHN is directly impacted by AD pathology. miR-132 replacement in adult mouse AD hippocampus restores AHN and relevant memory deficits. Our findings corroborate the significance of AHN in AD and reveal the possible therapeutic significance of targeting miR-132 in neurodegeneration.

Keywords

microRNA, miR-132, noncoding RNA, Alzheimer's disease, adult neurogenesis, dentate gyrus, memory, neurodegeneration, neural stem cells, neuronal precursors

Introduction

Substantial evidence has demonstrated that neurogenesis occurs in adult human brain, is impaired in Alzheimer's Disease (AD) patients and could contribute to the memory decline observed in AD

pathology (Boldrini et al., 2018; Cipriani et al., 2018; Gatt et al., 2019; Kempermann et al., 2018; Lucassen et al., 2019, 2020; Moreno-Jiménez et al., 2019; Mu and Gage, 2011; Tartt et al., 2018; Tobin et al., 2019). Cumulative data implicate adult neurons born at the subgranular zone of the dentate gyrus in a wide range of physiological mnemonic processes, including episodic, declarative, contextual and spatial memory, pattern separation, emotional control, functional forgetting and cognitive flexibility (Anacker and Hen, 2017; Baptista and Andrade, 2018; Toda et al., 2018). Pattern separation, a memory function that enables separation of similar representations into distinct, non-overlapping memories, is causally linked to the process of adult hippocampal neurogenesis (AHN) and is functionally dependent on the adult-born neurons in the rodent dentate gyrus (Clelland et al., 2009; Danielson et al., 2016; Sahay et al., 2011). Several studies have reported impaired performance in pattern separation tasks in patients with amnestic mild cognitive impairment (MCI) with increased rate of progression to clinically probable AD (Petersen et al., 2001) and also in late-stage AD patients (Ally et al., 2013; Wesnes et al., 2014; Yassa et al., 2010). Interestingly, higher numbers of neuroblasts in the dentate gyrus correlate with better ante-mortem cognitive status in MCI patients (Tobin et al., 2019), while proliferation and differentiation capacity of adult neural stem cells have been also correlated with memory performance in epilepsy patients (Coras et al., 2010).

A deeper understanding of the molecular mechanisms involved in AHN becomes particularly relevant when considering AHN as a therapeutic target for neurodegenerative diseases, like AD. Previously, we have shown that miR-132 regulates the timing for cell cycle exit of radial glia-like neural stem cells in the developing vertebrate spinal cord (Salta et al., 2014). miR-132 expression significantly increases during the transition from embryonic to larval stages to regulate Notch signaling via Ctbp2 downregulation and concurrent Sirt1 activation, thereby inducing neural stem cell differentiation. Much less is known about the role of miR-132 in adult rodent and human dentate gyrus, yet miR-132 expression is low in nestin-positive neural stem cells and progenitors, and gradually increases during the process of neuronal differentiation (Luikart et al., 2011). Moreover, miR-132 deletion in adult dentate gyrus induces significant alterations in neurite maturation, spine formation and synaptic

activity of newborn neurons, which compromises their functional integration into the adult hippocampal circuitry (Luikart et al., 2011; Magill et al., 2010). Interestingly, intersectional analysis of hippocampal transcriptomic profiles in miR-132-overexpressing and miR-132 conditional knockout mice reveals strong effects on genes involved in neurogenesis and cell proliferation (Hansen et al., 2016). Although no conclusive proof, these data suggest a possible role for miR-132 in adult neurogenesis under physiological conditions. Intriguingly, miR-132 is strongly and reproducibly downregulated in the hippocampus of human AD patients (Hebert et al., 2013; Lau et al., 2013; Patrick et al., 2017; Pichler et al., 2017; Salta and De Strooper, 2017; Salta et al., 2016; Smith et al., 2015; Wong et al., 2013; Zhu et al., 2016). miR-132 overexpression in primary neurons or mouse brain represses pathological hallmarks of AD, such as amyloid plaques, TAU hyperphosphorylation and deposition, and neuronal death (El Fatimy et al., 2018; Hernandez-Rapp et al., 2015; Salta et al., 2016; Smith et al., 2015; Wang et al., 2017; Wong et al., 2013; Zhu et al., 2016) (reviewed in (Salta and De Strooper, 2017)). However, the role of miR-132 in AHN in the context of AD remains elusive. Here, we report that miR-132 regulation is an integral and indispensable part of AHN and that miR-132 replacement restores AHN and memory deficits in two distinct mouse models of AD by exerting diverse effects at the adult hippocampal neurogenic niche.

Results

Adult hippocampal neurogenesis aberrations in AD parallel miR-132 deficiency in the dentate gyrus

In the subgranular zone, adult radial glia-like quiescent neural stem cells initially become activated, giving rise to transiently amplifying intermediate progenitors, which after limited rounds of proliferation generate fate-committed neuroblasts. Neuroblasts migrate tangentially along the subgranular zone and develop into immature neurons, which migrate radially into the granular cell layer to eventually mature into dentate granule neurons (Bond et al., 2015). Each of these activation and differentiation cellular states can be labeled with distinct markers (Figure 1A).

To obtain an independent proof-of-concept of AHN deficiency in AD, we first performed a postmortem human brain immunohistochemical analysis of proliferating neuronal progenitors at the subgranular zone of the dentate gyrus in tissue sections from 10 non-demented control individuals and 10 AD patients (Figure S1A). Normalized proliferating cell nuclear antigen $(PCNA)^+$-cell counts were significantly decreased by approximately 50% in AD dentate gyrus (Figure S1B). Astrocytes were negative for PCNA (Figures S1C, D), while $PCNA^+$-microglia were excluded based on their larger and less spherical shape compared to $PCNA^+$-neuronal precursor cells (Figures S1E, F). This reduction in the pool of proliferating cells, which eventually give rise to adult-born neurons, aligns with recent reports that provide strong evidence for decreased AHN in AD (Moreno-Jiménez et al., 2019; Tobin et al., 2019). Hence, miR-132 deficiency in the hippocampus of AD patients (Hebert et al., 2013; Lau et al., 2013; Patrick et al., 2017; Pichler et al., 2017; Salta and De Strooper, 2017; Salta et al., 2016; Smith et al., 2015; Wong et al., 2013; Zhu et al., 2016) parallels the decreased proliferation of neuronal precursors in the dentate gyrus.

We then asked whether miR-132 deficiency in AD is also functionally associated with the adult neurogenic niche. To address a possible genotype bias, we used two AD models, one overexpressing mutated forms of the human amyloid precursor protein (APP) and presenilin 1 (PS1) (*APP/PS1*) (Radde et al., 2006), and one carrying a knock-in mutated humanized *App* gene ($App^{NL\text{-}G\text{-}F}$) (Saito et al., 2014). The dentate gyrus of male wild-type (C57Bl/6), *APP/PS1* and $App^{NL\text{-}G\text{-}F}$ mice was microdissected and miR-132 levels were measured at different ages by real-time PCR (Figure 1B). We observed an early trend for miR-132 downregulation in AD dentate gyrus compared to wild-type, which became significant at 9 months in both the *APP/PS1* and the $App^{NL\text{-}G\text{-}F}$ animals. Similar changes were observed in female mice (Figure S1G). Since synaptic loss in the hippocampus might be a confounding variable contributing to the reduction of synaptic miR-132 levels (Edbauer et al., 2010), we assessed the expression levels of syntaxin 1A (*Stx1A*) and synaptophysin (*Syp*) as a proxy for synaptic integrity by real-time PCR (Dickey et al., 2003). No changes in the levels of these transcripts were observed at 12 months of age in wild-type or AD mouse dentate gyrus (Figure S1H). To dissect more subtle synaptic

alterations, we analyzed co-localizing presynaptic (VGlut1-positive) and postsynaptic (PSD95-positive) puncta in the granular cell layer, the molecular cell layer and the hilar area at 3 and 9 months of age. Only a modest decrease of synaptic puncta was observed in 9-month old *APP/PS1* and *App*$^{NL\text{-}G\text{-}F}$ dentate gyrus compared to age-matched wild-type animals (Figures S1I-K), suggesting that the robust miR-132 decline in old AD dentate gyrus is not primarily induced by synaptic loss.

We next investigated whether AHN is affected in the two AD mouse models. We employed incorporation of a synthetic analog of thymidine, bromodeoxyuridine (BrdU), in the DNA of cells undergoing mitosis, in mice exposed to voluntary running, which is a widely used paradigm for induction of neuronal progenitor proliferation and adult neurogenesis (van Praag et al., 1999). One month of voluntary running increased the number of proliferating neuronal precursor cells at the subgranular zone of the dentate gyrus of both wild-type and AD mice compared to sedentary controls at 3 and 6 months of age (Figures 1C, E). However, the potential to induce neuronal progenitor proliferation at the subgranular zone upon running was compromised in 9-month old AD dentate gyrus, as opposed to wild-type mice (Figures 1C, E). Notably, this was paralleled by changes in miR-132 expression in the dentate gyrus. miR-132 levels significantly increased in running mice of all three genotypes at 3 and 6 months, yet no change was observed in running AD mice at 9 months of age (Figure 1D). Thus, adult neurogenesis and miR-132 induction drop in the aging AD mice. miR-212, a cognate microRNA of miR-132 which is co-transcribed from the same genetic locus, did not potently respond to physical exercise at any of the assessed time points in any of the genotypes (Figure S1L).

Taken together, these results point towards a possible correlation between an amyloid plaque or amyloid beta (Aβ) oligomer pathology-induced effect on miR-132 expression and compromised AHN in two different mouse models for amyloid plaque pathology in Alzheimer's disease.

miR-132 expression at the adult hippocampal neurogenic niche is affected by amyloid beta pathology

We next assessed miR-132 localization in the adult neurogenic niche. One technical problem here is the strong baseline expression of miR-132 in the granule neurons of the dentate gyrus, which could mask the overall lower expression of miR-132 in cells at the subgranular zone (Luikart et al., 2011). We therefore used a nestin promoter-based green fluorescent protein (Nestin:GFP) reporter line in conjunction with additional markers to label neural stem cells and neuronal precursors at the subgranular zone of the dentate gyrus (Mignone et al., 2004) and employed fluorescence *in situ* hybridization and fluorescence-activated cell sorting (FACS) to determine the expression of miR-132. We use the term 'Nestin:GFP$^+$-niche cells' to collectively refer to the GFP-positive dentate gyrus populations (Artegiani et al., 2017; Shin et al., 2015). Fluorescence *in situ* hybridization revealed that at basal conditions miR-132 is expressed in Nestin:GFP$^+$/Ki-67$^+$-proliferating neuronal precursor cells (Figure 2A) and Nestin:GFP$^+$/Dcx$^+$-immature neurons (Figure 2B) at the subgranular zone. Hybridization with a scrambled probe was used as a negative control (Figures S2A, B). Using a more quantitative method, we next confirmed detection by real-time PCR and assessed the time course of miR-132 expression in Nestin:GFP$^+$-niche cells isolated from wild-type mouse dentate gyrus. miR-132 levels were detectable in Nestin:GFP$^-$- and to a smaller extent in Nestin:GFP$^+$ -populations already at 1.5 month of age (Figure 2C). We observed a significant and specific increase of miR-132 expression in sorted cells at 12-months (Figures 2C and S2C). Interestingly, miR-132 upregulation did not occur in the Nestin:GFP$^-$ -fraction which mainly consists of granule dentate neurons (Figure 2C), indicating that miR-132 is upregulated in the neurogenic niche, but not in the mature neurons, over time. Moreover, induction of adult neurogenesis via physical exercise elicited a significant upregulation of miR-132 only in the Nestin:GFP$^+$-niche cell fraction (Figures 2D) and not in the Nestin:GFP$^-$-neuronal population (Figure 2E). This upregulation was specific for miR-132 as the levels of miR-212 and of miR-124, a brain-enriched microRNA, were not changed (Figures S2D-G). We then asked whether amyloid plaque pathology affects miR-132 levels at the hippocampal neurogenic niche. To address this question, we crossed Nestin:GFP with *App*$^{NL\text{-}G\text{-}F}$ (Nestin-NLGF) mice and measured miR-132 levels in GFP$^+$- and GFP$^-$-cells isolated from the dentate gyrus at different ages. miR-132 levels in the Nestin:GFP$^+$-niche cells of

the AD mouse dentate gyrus increased at 6 months of age, similarly to wild type mice, but sharply decreased at 9 months (Figures 2F, S2I) coinciding with the inability of the neuronal progenitors in the AD mouse model brain to proliferate upon running. No significant changes were observed for miR-212 (Figure S2H). Taken together, these data show that miR-132 is recruited by adult neural stem cells and progenitors as part of the response to exercise- or aging- related stimuli, but fails to do so upon exposure to Aβ pathology in the hippocampal neurogenic niche.

miR-132 is required for proliferation of neural precursors and neuronal differentiation in adult dentate gyrus

We then asked whether miR-132 is required for adult neurogenesis in wild-type dentate gyrus. As expected, voluntary running induced an increase in the numbers of $BrdU^+$- and $Ki\text{-}67^+$-proliferating neuronal precursors, $Nestin{:}GFP^+$-neural stem cells and progenitors, and DCX^+-immature neurons at the subgranular zone of the dentate gyrus in scramble control-injected wild-type mice compared to sedentary animals (Figures 3A-F). However, the effect of physical exercise on AHN was abrogated by miR-132 knockdown (Figure S3A) in running mice intracerebroventricularly (ICV)-injected with an antisense oligonucleotide against miR-132 (AntagomiR-132, Ant-132) (Figures 3A-F), demonstrating that miR-132 is required for the induction of AHN by running. miR-132 knockdown was confirmed in both the $Nestin{:}GFP^+$- and the $Nestin{:}GFP^-$ -fractions of the neurogenic niche (Figure S3B) and was specific to miR-132 (Figure S3C). Immunostaining against the proliferation marker PCNA confirmed that miR-132 knockdown abolishes the positive effect of running on neuronal precursor proliferation (Figures S3D, E). Since miR-132 is also involved in the regulation of neuronal apoptosis (Wong et al., 2013), we asked whether the net effect of miR-132 knockdown could be mediated by interfering with the physiological process of neuronal progenitor elimination by apoptotic death. Quantification of the cells labeled by an antibody against cleaved caspase-3, a marker of apoptosis, did not reveal any significant changes between groups (Figures S3F, G), indicating that miR-132 regulation of AHN is not effectuated at the level of apoptotic control. Interestingly, miR-132 deficiency also impaired the

exercise-induced elevation of Brain-Derived Neurotrophic Factor (*Bdnf)* (Figure S3H), which has recently emerged as an essential neurotrophin for the fitness of the adult hippocampal neurogenic niche and the cognitive recovery in an AD mouse model (Choi et al., 2018).

To obtain a measurement of the global effect of miR-132 deficiency on the neural stem cells and progenitors *in vivo*, we employed tissue clearing to assess the numbers of the Nestin:GFP^{+}-cells at the subgranular zone of the whole dentate gyrus (Figures 3G-I). We compared the numbers of Nestin:GFP^{+}-neural stem cells and progenitors at the subgranular zone of running mice (Figures 3J-L) injected either with scramble control- (Video S1) or with Ant-132 (Video S2). miR-132 knockdown resulted in a small but significant decrease in the total number of neural stem cells and progenitors (Figure 3J), confirming our previous observations. Together, these data unequivocally demonstrate that miR-132 is required for the induction of neurogenesis in the dentate gyrus *in vivo*.

miR-132 regulates neuronal differentiation and is downregulated by AD-related pathology in human neural stem cells

We next assessed whether miR-132 regulation is also involved in the differentiation of human neuronal precursor to neurons. miR-132 levels significantly increased by 20-fold upon neural induction of primary human embryonic stem cells to neuronal precursors and were further boosted by more than 300-fold during neuronal maturation (Figures 4A, B). miR-212 levels, in contrast, were only subtly altered over the course of neuronal differentiation and maturation (Figure S4A). The progression of neuronal differentiation was monitored by measuring beta tubulin 3 (TUBB3) mRNA levels (Figure 4C). A similar upregulation of miR-132 was detected in an immortalized human neural stem cell and progenitor line of mesencephalic origin (RenCells VM) upon induction of neuronal differentiation (Figures 4D, E), providing further support for the functional significance of miR-132 in the process of human neurogenesis. The differentiation efficiency was monitored by immunostaining for NESTIN and SOX2 (neural stem cells), Ki-67 (proliferating neuronal precursor cells) and TUBB3 (mature neurons) (Figures S4B, C). The levels of TUBB3 were additionally measured by semi-quantitative real-time PCR

(Figure 4E). Notably, miR-132 transfection in human undifferentiated RenCell neural stem cells and progenitors (Figures S4D, E) resulted in a significant upregulation of TUBB3 (Figures 4F, S4J), suggesting that miR-132 is a positive regulator of neurogenesis in human neuronal progenitors. A ten times lower miR-132 dose (Figure S4F) had an overall milder yet still significant effect on the levels of TUBB3 (Figure S4G). Conversely, miR-132 knockdown in differentiating RenCell neural stem cells and progenitors (Figures S4H, I) induced a decrease of TUBB3 levels (Figures 4G, S4K). Similar results were obtained upon miR-132 overexpression (Figure 4H, I) and knockdown (Figure 4J) in human neural precursor cells of hippocampal origin (HPC0A07/03C), corroborating the relevance of miR-132 regulation over human neurogenesis.

To explore whether Aβ pathology can prompt miR-132 downregulation in human neural stem and progenitor cells, we treated human embryonic stem cell-derived neuronal precursor cells with $A\beta_{1-42}$ oligomers. Incubation of these cells with 5 μM $A\beta_{1-42}$ for 72 h impacted their proliferation capacity (Figure 4K) and induced a specific miR-132 decrease compared to cells incubated with a scramble control (Figures 4K, S4L). The hippocampal neurogenic niche is highly vascularized and hence permissive to molecular cues transmitted via communication with the systemic environment (Villeda et al., 2011). Previously, it was shown that incubation of human neuronal precursor cells of hippocampal origin with serum samples derived from AD patients compared to non-demented control individuals reduced cell proliferation (Maruszak et al, 2017, BioRxiv 10.1101/175604). We extend this observation here by demonstrating that neuronal precursor cells treated with sera derived from AD patients showed significantly reduced miR-132, but not miR-212, levels (Figures 4L, S4M), while incubation with the AD sera also impacted cell proliferation (Figure 4L). These data confirm that miR-132 expression is suppressed in human stem cells by Aβ oligomers or other AD-related serum-derived factors.

miR-132 alleviates proliferation and differentiation deficits of adult neural precursors in AD mouse model brain

We next investigated whether boosting miR-132 levels could ameliorate the AHN deficits that we observed in the two AD mouse models. Control-injected 9-month old *APP/PS1* mice were not able to induce AHN upon running, as assessed by the numbers of $BrdU^+$-, $Ki\text{-}67^+$-proliferating neuronal precursor cells, and DCX^+-immature neurons at the subgranular zone of the dentate gyrus (Figures 5A-D). However, upon miR-132 overexpression via ICV injection of a synthetic miR-132 mimic oligonucleotide (Figure S5A), we observed significant increases in these cell populations under sedentary conditions. Similar results were obtained in the $App^{NL\text{-}G\text{-}F}$ male (Figures 5E-H and S5B) and $App^{NL\text{-}G\text{-}F}$ female mice (Figures S5C, D), suggesting that this was not a strain- or gender-dependent effect. To assess whether the apparent increase in proliferating progenitors and immature neurons is the result of an intrinsic transcriptional response of the resident niche cells to miR-132 and to account for the variation in cell numbers between miR-132-overexpressing and control animals, we measured the levels of markers of stemness (*Pax6*), cell proliferation (*Mki67*) and early neuronal fate (*Dcx*) in equal numbers of sorted $Nestin{:}GFP^+$ -cells isolated from the dentate gyrus of miR-132- or control-injected mice (Figures 5I, S6A). miR-132 overexpression significantly repressed early stem cell identity in this pool of cells and induced transcriptomic changes indicative of increased proliferation and differentiation rates.

Cell-autonomous regulatory effects of miR-132 in adult neural stem cells and progenitors at the AD mouse hippocampal niche

Considering that ICV infusion of miR-132 mimic oligonucleotides may exert broad effects in different cell types at the adult hippocampal niche, we deployed two distinct strategies to overexpress miR-132 specifically in adult neural stem cells (NSC) and their progeny in the dentate gyrus of $App^{NL\text{-}G\text{-}F}$ mice (Figure 6A).

First, a lentiviral vector (LV PGK:mCHERRY) expressing an mCHERRY reporter and a miR-132-overexpressing hairpin under the control of the PGK promoter (Suh et al., 2018) was used for stereotactic injections into the dentate gyrus. Considering the possibility that LV PGK:mCHERRY, apart

from adult NSCs, may also transduce a proportion of developmentally born granule cells, we additionally employed a retroviral approach to target miR-132 overexpression to proliferating adult neuronal precursors in a second mouse cohort. More specifically, we used a standard retroviral system expressing the miR-132 hairpin cassette and a GFP reporter under the CAG promoter (RV CAG:GFP) (Zhao et al., 2006). The efficiency of miR-132 overexpression was assessed in the dentate gyrus of mice injected with the two hairpin constructs compared to the two corresponding control vectors (Figure 6B, C).

Morphometric dendritic features in adult-born granule neurons are correlated to functional integration and connectivity (van Praag et al., 2002; Trinchero et al., 2017; Zhao, 2006). We analyzed dendritic development in 4-week old neurons, a time point at which these cells are functionally integrated (van Praag et al., 2002; Zhao, 2006). Consistent with the AHN deficits observed earlier, no running-induced effects were observed in the dendritic length and arbor complexity of labelled granule cells in *App*$^{NL-G-F}$ mice injected with either the lentiviral or the retroviral control vectors 4 weeks post injection (Figure 6D-G). However, both lentiviral and retroviral miR-132 overexpression reversed these deficits in the neuronal progeny under both sedentary and running conditions (Figure 6D-G).

Synaptic integration of the developing adult-born granule neurons follows a stereotypic sequence, starting with the formation of GABAergic dendritic inputs and followed by glutamatergic synaptogenesis and formation of dendritic spines (Trinchero et al., 2017). At 4 weeks of age, newly born neurons already receive excitatory input from the perforant path, which connects the dentate gyrus to the entorhinal cortex (van Praag et al., 2002). Both lentiviral and retroviral miR-132 overexpression in *App*$^{NL-G-F}$ granule cells 4 weeks post injection, significantly increased spine density, as opposed to running, which had no effect (Figure 6H-K).

Together, these data suggest that miR-132 regulates late-stage neuronal maturation in a cell-autonomous manner, and that increasing miR-132 in adult neural stem cells and progenitors can ameliorate deficits in the dentate gyrus of an AD mouse model.

miR-132 promotes AHN by modulating a complex molecular network in adult neural stem cells

In order to identify the mechanisms underpinning the positive regulatory effect of miR-132 in AHN, we employed a single-cell RNA-sequencing approach to assess miR-132-specific transcriptomic responses in the Nestin:GFP-labeled resident niche cells (Figure 7A). Nestin:GFP$^+$-niche cells were isolated from dentate gyri of mice that were ICV-injected with either miR-132 mimic or control oligonucleotides and single-cell libraries were prepared as discussed in the STAR Methods section. The extent and specificity of miR-132 overexpression was assessed in Nestin:GFP$^+$ and Nestin:GFP$^-$ bulk-sorted cells (Figure S6A). While miR-132 levels were, as expected, elevated in both populations compared to control-injected animals, the increase was only significant in the Nestin:GFP$^+$ fraction (Figure S6A), which may reflect the relative high baseline expression of miR-132 in the neuronal fraction of the dentate gyrus. A total of 709 Nestin:GFP$^+$ single niche cells were sequenced using the Smart-seq2 protocol. Unsupervised hierarchical clustering of the dataset using the Seurat algorithm revealed 7 populations, which were projected on a t-distributed stochastic neighbor embedding (t-SNE) map for visualization (Figure 7B). Based on the expression levels of well-characterized marker genes (Artegiani et al., 2017; Hochgerner et al., 2018; Zeisel et al., 2018) (Table S5; LiteratureMarkers), we defined cluster identity (Figures 7B, S6B and Table S5; ModuleScore), mapping the subpopulations as radial glia-like (RGL) neural stem cells, neuronal intermediate precursor cells (NPC), astrocytes, oligodendrocyte precursor cells (OPC), myelin-forming oligodendrocytes (MFOL), endothelial cells and pericytes. Cell type-enriched genes were identified by comparing each cell type cluster to all others (Figure S6C and Table S5; ClusterMarkers). The distribution of cells across clusters was not altered in a statistically significant way upon miR-132 overexpression in these experiments (data not shown).

Differential gene expression analysis between miR-132-overexpressing and control cells within each cluster did not reveal any significantly deregulated transcripts after correction for multiple testing comparisons (Table S6), an observation that could be indicative of the frequently documented limited effect sizes of microRNA regulation (Moore et al., 2015). Since microRNAs may elicit changes on cellular

dynamics via widespread, yet subtle effects on the transcriptome (Liufu et al., 2017), we next assessed the possible impact of miR-132 overexpression on molecular pathway regulation through gene set analysis. Gene ontology (GO) enrichment analysis using Ingenuity Pathway Analysis (IPA, Ingenuity Systems Inc., Redwood City, CA, USA) identified significantly enriched pathways upon miR-132 overexpression in each of the seven cell subpopulations (Figure S6D), suggesting that miR-132 regulation, although subtle at the single-gene level, may concomitantly impact diverse cellular processes. To gain empirical support for this notion, we used the human RenCell line to validate putative miR-132 targets. To prioritize possible direct targets, we selected 150 of the most downregulated transcripts in single neural stem cells (radial glia-like cells) upon miR-132 overexpression. Using three prediction algorithms for miRNA target identification (Targetscan, DIANA, PicTar), we extracted a list of 52 predicted miR-132 targets (predicted at least by one of the three algorithms) for semi-quantitative real-time PCR validation in RenCells transfected with either a miR-132 mimic or a control oligonucleotide. Interestingly, there was a significant change in the levels of five mRNAs i.e. *DOCK1* (Dedicator Of Cytokinesis 1), *EPHB3* (EPHrin receptor B3), *BTG2* (B-cell Translocation Gene anti-proliferation factor 2), *CAMK1* (Calcium/Calmodulin-Dependent Protein Kinase 1) and *RAC1* (RAs-related C3 botulinum toxin substrate 1), which were all found to be downregulated (Figure 7C), suggesting that these transcripts may be part of the direct effectors of the miR-132-regulated molecular network that generates proneurogenic signals in the radial glia-like neural stem cells.

Boosting miR-132 levels restores AHN-related memory deficits in old AD mice

AHN has been linked to the memory processing ability of the hippocampal circuitry and to several mnemonic processes, including contextual memory and, in particular, pattern separation (Clelland et al., 2009; Suárez-Pereira et al., 2015). To address the functional impact of AHN regulation by miR-132 on relevant memory functions, we assessed the effect of miR-132 overexpression in 9-month old App^{NL-G-F} mice in a passive avoidance test and in a pattern separation, differential fear conditioning-based

test (van Boxelaere et al., 2017). Age-matched wild-type mice were used as controls and animals were ICV-injected with either a negative control oligonucleotide or a synthetic miR-132 mimic before behavioral testing (Figure S5E). In passive avoidance, AD mice exhibited decreased latency time to enter the conditioning chamber compared to wild-type animals during the testing phase, suggesting impaired contextual memory (Figure 8A). No change was observed between controls and miR-132-overexpressing wild-type mice (Figure 8A). Interestingly, boosting miR-132 levels in the AD mice rescued this deficit and restored latency time to wild-type levels (Figure 8A). In contrast, after repeated contextual conditioning in a pattern separation test (Figures 8B, C), AD mice showed similar contextual fear memory as wild-type animals, and elevating miR-132 levels had no effect on contextual discrimination between two very distinct contexts (Figure 8D, contexts A and C). These results indicate that repeated conditioning establishes context-specific memory traces also in the AD animals, while boosting miR-132 levels has no effect on specific contextual memory. However, discriminating between highly similar contexts (contexts A and B) relies on pattern separation, which is dependent upon the firing properties of the adult-born neurons in the dentate gyrus. In this test, wild-type controls displayed discriminatory levels of freezing in contexts A and B, while AD animals were unable to distinguish between the two overlapping contexts (Figure 8E). Interestingly, miR-132 overexpression in App^{NL-G-F} mice restored performance in the pattern separation test (Figure 8E), suggesting that the positive regulation of AHN by miR-132 can promote cognitive recovery in AD. However, overexpressing miR-132 in wild-type mouse brain resulted in poor performance compared to the control-injected group (Figure 8E), which could indicate a possible requirement for a dose window for the miR-132 positive effect.

We then addressed the possible contribution of AHN to the beneficial effect of miR-132 in the passive avoidance test in the AD mice. We used the DNA-alkylating agent temozolomide (TMZ), which has been previously shown to repress AHN and context discrimination (Egeland et al., 2017; Garthe et al., 2009; McAvoy et al., 2016; Niibori et al., 2012), to block cell proliferation in control- and miR-132-injected App^{NL-G-F} mice (Figure 8F). Ki-67^{+}- and Dcx^{+}- cell counts at the subgranular zone of the dentate

gyrus were used as a readout of the efficiency of proliferation inhibition of adult NPCs (Figures 8G, H, S5F, G). Blocking proliferation in miR-132-overexpressing AD mice abolished memory rescue in the passive avoidance task (Figure 8I), thereby providing indirect evidence that AHN may be a prime component of miR-132 regulation on contextual memory performance in this task. These results suggest that replacing miR-132 levels in the AD brain can restore AHN-related memory deficits.

Discussion

Downregulation of miR-132 expression is a consistent observation in brain samples of Alzheimer's disease patients (Hebert et al., 2013; Lau et al., 2013; Patrick et al., 2017; Pichler et al., 2017; Salta and De Strooper, 2017; Salta et al., 2016; Smith et al., 2015; Wong et al., 2013; Zhu et al., 2016). We demonstrate here significant reduction of miR-132 levels in the adult hippocampal neurogenic niche in two different amyloidosis mouse models for AD and confirm downregulation of miR-132 in two different *in vitro* models for human neuronal stem cell differentiation upon treatment with synthetic Aβ oligomers or serum from AD patients. We link these defects to impaired AHN in the two AD mouse models by showing that intracerebroventricular infusion of synthetic miR-132 oligonucleotides or selective overexpression of miR-132 in adult neuronal stem cells and progenitors rescues the AHN deficits and additionally restores aspects of memory dysfunction. Our work suggests that loss of miR-132 is an important contributor to the overall decreased AHN in Alzheimer's patients (Moreno-Jiménez et al., 2019; Tobin et al., 2019) and provides evidence that restoring miR-132 levels in the adult hippocampal neurogenic niche might be beneficial in AD.

Whether AHN is affected in AD brain and, even more fundamentally, whether AHN occurs in adult and aging human brain at all, has been a returning issue of controversy (Boldrini et al., 2018; Eriksson et al., 1998; Gatt et al., 2019; Kempermann et al., 2018; Knoth et al., 2010; Lucassen et al., 2019, 2020; Paredes et al., 2018; Snyder, 2019; Sorrells et al., 2018; Spalding et al., 2013; Tartt et al., 2018). The discussion has taught the paramount importance of accurate interpretation of histological findings, sample stratification (to minimize confounding factors such as agonal state, coexisting brain pathology,

neuroinflammation, medication), postmortem delay, tissue preservation, marker labeling methodology, and inclusion of stereology during data analysis (Kempermann et al., 2018; Lucassen et al., 2019, 2020). Notably, two recent reports using high-quality human postmortem brain samples and refined methodological approaches have now firmly established that adult neurogenesis occurs in human brain. These studies demonstrated that AHN can still be detected in centenarians, and that AHN drops dramatically in AD patients (Moreno-Jiménez et al., 2019; Tobin et al., 2019), setting the stage for the functional studies in two mouse models of AD reported here.

We show that the running-induced miR-132 upregulation in the hippocampal neurogenic niche becomes compromised with pathology progression, independently of gender, and that these alterations are paralleled by decreased neurogenic potential. The hippocampal neurogenic niche involves a complex network of intercellular communication and molecular regulatory signals, which is receptive to extrinsic and intrinsic cues, such as experience, exercise, aging and increased neuroinflammation (Fuster-Matanzo et al., 2013; Mosher and Schaffer, 2018; Villeda et al., 2011). Our data demonstrate that treatment of human neuronal precursor cells with oligomeric Aβ reduces proliferation and miR-132 expression, consistent with several lines of evidence suggesting that Aβ *per se* impacts the neurogenic potential of neural stem cells and progenitors (Haughey et al., 2002; He et al., 2013; Lee et al., 2013). Serum obtained from sporadic AD cases also elicited a significant reduction of miR-132 in hippocampal human neural stem cells. This can be attributed to Aβ oligomers or other AD-related systemic signals.

In an attempt to identify relevant transcriptomic targets of miR-132 at the adult hippocampal neurogenic niche, we performed single-cell transcriptome analysis of the Nestin:GFP-positive niche-residing cells, isolated from the dentate gyrus of mice overexpressing miR-132. Although these studies revealed trends for regulation of transcripts in several cell types, they did not reach statistical significance. The inherent challenges of characterizing direct microRNA targets is well acknowledged (Liufu et al., 2017) and likely reflect the subtle pleiotropic roles of miR-132 in the adult neurogenic niche. Given these limitations, we decided to validate possible regulatory interactions in human neural

stem cells *in vitro*. This approach revealed a novel miR-132-specific molecular signature consisting of *DOCK1, EPHB3, BTG2, CAMK1* and *RAC1*, all of which have reported roles in neuronal differentiation and function (Fortin et al., 2010; Goold and Nicoll, 2010; Pillat et al., 2016; Theus et al., 2010; Vadodaria et al., 2013; Yang et al., 2012). Dock1, Ephb3, Camk1 and Rac1 have additionally been implicated in AD (Aguilar et al., 2017; Becker et al., 2014; Overk and Masliah, 2014; Riascos et al., 2014), while all five proteins have been associated with the immune response in a variety of cells (D'Ambrosi et al., 2014; Goold and Nicoll, 2010; Guo et al., 2013; Naskar et al., 2014; Pillat et al., 2016; Theus et al., 2010; Yuniati et al., 2018). Interestingly, miR-132 knockdown also repressed the running-induced increase of *Bdnf*, a key neurotrophic factor contributing to the fitness of the niche and the neurogenic potential. Of note, miR-132 overexpression in human neuronal precursors *in vitro* and adult mouse neural stem cells and progenitors *in vivo* induced neuronal differentiation and maturation in a cell-autonomous manner. Collectively, these observations suggest that the proneurogenic effects of miR-132 may be effectuated at the level of NPC proliferation, neuronal differentiation, survival, functional integration, neurotrophic boost or a combination thereof, possibly depending on the presence or absence of distinct stimuli.

Adult-born neurons can modulate and sparsify activity in the dentate gyrus. They act as autonomous coding units with unique electrophysiological properties, thereby enabling the hippocampus to optimize memory resolution and robustness (Johnston et al., 2016). These newly born cells facilitate the spatiotemporal contextualization of information and they help avoid catastrophic interference in the hippocampal network, by promoting 'behavioral pattern separation' (Kempermann et al., 2018). They may also contribute directly or indirectly to forgetting and memory clearance, memory consolidation and spatiotemporal contextualization (Gonçalves et al., 2016). Poor performance in pattern separation tasks in AD patients (Ally et al., 2013; Wesnes et al., 2014; Yassa et al., 2010) and preserved AHN in non-demented individuals with AD or MCI neuropathology have been reported (Briley et al., 2016; Tobin et al., 2019). While a comprehensive analysis of the relationship between miR-132, deficient AHN and memory would require a separate study, we confirm here that features of

hippocampus-dependent functions that are related to context fear conditioning and avoidance tasks, which are linked to deficient AHN in the context of an AD mouse model, can be rescued by restoring miR-132 levels in the brain of these mice.

Intriguingly, miR-132 overexpression in wild-type mice resulted in a worsening of performance in the AHN-specific pattern separation task, suggesting that miR-132 expression should be maintained within a certain range to ensure proper learning and memory function. Indeed, while miR-132 levels are approximately 1.5-fold induced in mouse hippocampus upon presentation with a spatial memory task (Hansen et al., 2013), higher (>3-fold) levels inhibit hippocampus-dependent memory in wild type mice (Hansen et al., 2013). Our approach yielded a miR-132 overexpression of approximately 4-fold in the dentate gyrus of old wild-type and AD mice, which improved the memory deficits in the AD mice but interfered with learning and memory in the wild-type animals. Thus, further work is required to assess a therapeutically relevant window for miR-132 overexpression in AD brain.

In conclusion, our data support a model where miR-132 acts as a proneurogenic signal transducer contributing to specific aspects of memory formation. AD pathology leads to miR-132 deficiency and ultimately compromises AHN. Recently, induction of AHN in conjunction with improvement of the microenvironment of the adult hippocampal niche via BDNF overexpression was put forward as a putative target for therapeutic intervention in AD (Choi et al., 2018). Moreover, recent groundbreaking advances in the treatment of neurodegenerative disorders using small RNA-based therapeutics in spinal muscular atrophy (Finkel et al., 2016) may also pave the way for more direct novel miR-132-based therapeutic approaches in AD. Dose finding will be crucial, while delineating the molecular and cellular mechanisms underlying the neurogenic effects of miR-132 may provide impetus for identifying novel strategies to therapeutically harness AHN in AD.

Acknowledgements

We thank Véronique Hendrickx and Jonas Verwaeren for animal husbandry; Sebastian Munck, Nikky Corthout, Axelle Kerstens (LiMoNe, VIB), the VIB Nucleomics Core of Leuven, the VIB-KU Leuven FACS

Core, An Snellinx, Isabel Salas, Dries T'Syen, Sara Calafate, Jeroen Vanderlinden, Natalia Gunko, Dorien Vandael, Annette Gärtner and Jenny Peeters for providing technical assistance and resources; Annerieke Sierksma, Patrik Verstreken, Laure Bally-Cuif, Joris De Wit, Pierre Vanderhaeghen and Matthew Holt for critical discussions and feedback. The *APP/PS1* mice were a kind gift from Mathias Jucker, DZNE, Germany, the App^{NL-G-F} mice were kindly provided by Takaomi Saido, RIKEN Brain Science Institute, Japan, and the Nestin:GFP mice from Grigori Enikolopov, Stony Brook University, NY, USA. The PGK lentiviral vector was a kind gift from Antonella Consiglio. Confocal microscope equipment was acquired through a Hercules Type 1 AKUL/09/037 to Wim Annaert and a CLME grant to the VIB BioImaging Core. HW is a Fonds voor Wetenschappelijk Onderzoek (FWO) Scholar and receives funding from B-SMART EU Horizon2020 and Stichting Alzheimer Onderzoek (SAO). DRT is funded by grants from FWO (G0F8516N Odysseus) and Vlaamse Impulsfinanciering voor Netwerken voor Dementie-onderzoek (IWT 135043). The work in the ST lab is supported by UK Medical Research Council grants MR/N030087/1 and MR/S00484X/1. HZ is a Wallenberg Scholar. Work in the BDS laboratory is supported by a European Research Council (ERC) grant ERC-2010-AG_268675, FWO, KU Leuven, VIB, SAO, the Elisabeth Foundation, VIND (IWT 135043), and a Methusalem grant from KU Leuven and the Flemish Government. BDS is the Bax-Vanluffelen Chair for Alzheimer's Disease and is supported directly by the Opening the Future campaign of the Leuven Universiteit Fonds. ES has previously received funding from FWO, Alzheimer's Association (AA) and SAO. Work in the ES lab is currently supported by Alzheimer Nederland, Health Holland and AA.

Author contributions

Conceptualization, HW, BDS and ES; Methodology, HW, SB, KC, LW, ZCV, RDH, DRT, ESi, ST, CSF, BDS and ES; Investigation, HW, SB, SS, EVE, KC, KH, LW, AR, ESi, AP, GT, CSF and ES; Software, MF, NT, YF; Formal Analysis, MF, NT, YF and ES; Resources, ZCV, RDH, DRT, HZ, ST; Writing – Review & Editing, ES and BDS, with input from all authors; Supervision, ES, BDS; Funding Acquisition, ES and BDS.

Declaration of interests

The authors declare no competing interests related to this work.

References

Aguilar, B.J., Zhu, Y., and Lu, Q. (2017). Rho GTPases as therapeutic targets in Alzheimer's disease. Alzheimers. Res. Ther. *9*, 97.

Ally, B.A., Hussey, E.P., Ko, P.C., and Molitor, R.J. (2013). Pattern separation and pattern completion in Alzheimer's disease: Evidence of rapid forgetting in amnestic mild cognitive impairment. Hippocampus *23*, 1246–1258.

Anacker, C., and Hen, R. (2017). Adult hippocampal neurogenesis and cognitive flexibility — linking memory and mood. Nat. Rev. Neurosci. *18*, 335–346.

Artegiani, B., Lyubimova, A., Muraro, M., van Es, J.H., van Oudenaarden, A., and Clevers, H. (2017). A Single-Cell RNA Sequencing Study Reveals Cellular and Molecular Dynamics of the Hippocampal Neurogenic Niche. Cell Rep. *21*, 3271–3284.

Baptista, P., and Andrade, J.P. (2018). Adult Hippocampal Neurogenesis: Regulation and Possible Functional and Clinical Correlates. Front. Neuroanat. *12*.

Becker, T., Ramirez, A., Herold, C., van Duijn, C., Schellenberg, G.D., Williams, J., Amouyel, P., Yang, Q., Seshadri, S., and van der Lee, S.J. (2014). COMPREHENSIVE GENE-GENE INTERACTION META-ANALYSIS OF IGAP GWA STUDIES. Alzheimer's Dement. *10*, P245.

Boldrini, M., Fulmore, C.A., Tartt, A.N., Simeon, L.R., Pavlova, I., Poposka, V., Rosoklija, G.B., Stankov, A., Arango, V., Dwork, A.J., et al. (2018). Human Hippocampal Neurogenesis Persists throughout Aging. Cell Stem Cell *22*, 589–599.e5.

Bond, A.M., Ming, G., and Song, H. (2015). Adult Mammalian Neural Stem Cells and Neurogenesis: Five Decades Later. Cell Stem Cell *17*, 385–395.

van Boxelaere, M., Clements, J., Callaerts, P., D'Hooge, R., and Callaerts-Vegh, Z. (2017). Unpredictable chronic mild stress differentially impairs social and contextual discrimination learning

in two inbred mouse strains. PLoS One *12*, e0188537.

Briley, D., Ghirardi, V., Woltjer, R., Renck, A., Zolochevska, O., Taglialatela, G., and Micci, M.-A. (2016). Preserved neurogenesis in non-demented individuals with AD neuropathology. Sci. Rep. *6*, 27812.

Brkic, M., Balusu, S., Van Wonterghem, E., Gorle, N., Benilova, I., Kremer, A., Van Hove, I., Moons, L., De Strooper, B., Kanazir, S., et al. (2015). Amyloid Oligomers Disrupt Blood-CSF Barrier Integrity by Activating Matrix Metalloproteinases. J. Neurosci. *35*, 12766–12778.

Butler, A., Hoffman, P., Smibert, P., Papalexi, E., and Satija, R. (2018). Integrating single-cell transcriptomic data across different conditions, technologies, and species. Nat. Biotechnol. *36*, 411–420.

Callaerts-Vegh, Z., Ahmed, T., Vermaercke, B., Marynen, P., Balschun, D., Froyen, G., and D'Hooge, R. (2015). Nxf7 deficiency impairs social exploration and spatio-cognitive abilities as well as hippocampal synaptic plasticity in mice. Front. Behav. Neurosci. *9*.

Choi, S.H., Bylykbashi, E., Chatila, Z.K., Lee, S.W., Pulli, B., Clemenson, G.D., Kim, E., Rompala, A., Oram, M.K., Asselin, C., et al. (2018). Combined adult neurogenesis and BDNF mimic exercise effects on cognition in an Alzheimer's mouse model. Science (80-.). *361*, eaan8821.

Cipriani, S., Ferrer, I., Aronica, E., Kovacs, G.G., Verney, C., Nardelli, J., Khung, S., Delezoide, A.-L., Milenkovic, I., Rasika, S., et al. (2018). Hippocampal Radial Glial Subtypes and Their Neurogenic Potential in Human Fetuses and Healthy and Alzheimer's Disease Adults. Cereb. Cortex *28*, 2458–2478.

Clelland, C.D., Choi, M., Romberg, C., Clemenson, G.D., Fragniere, A., Tyers, P., Jessberger, S., Saksida, L.M., Barker, R.A., Gage, F.H., et al. (2009). A Functional Role for Adult Hippocampal Neurogenesis in Spatial Pattern Separation. Science (80-.). *325*, 210–213.

Coras, R., Siebzehnrubl, F.A., Pauli, E., Huttner, H.B., Njunting, M., Kobow, K., Villmann, C., Hahnen, E., Neuhuber, W., Weigel, D., et al. (2010). Low proliferation and differentiation capacities of adult hippocampal stem cells correlate with memory dysfunction in humans. Brain *133*, 3359–3372.

D'Ambrosi, N., Rossi, S., Gerbino, V., and Cozzolino, M. (2014). Rac1 at the crossroad of actin dynamics and neuroinflammation in Amyotrophic Lateral Sclerosis. Front. Cell. Neurosci. *8*, 279.

D'Hooge, R. (2005). Neurocognitive and Psychotiform Behavioral Alterations and Enhanced Hippocampal Long-Term Potentiation in Transgenic Mice Displaying Neuropathological Features of Human -Mannosidosis. J. Neurosci. *25*, 6539–6549.

Danielson, N.B., Kaifosh, P., Zaremba, J.D., Lovett-Barron, M., Tsai, J., Denny, C.A., Balough, E.M., Goldberg, A.R., Drew, L.J., Hen, R., et al. (2016). Distinct Contribution of Adult-Born Hippocampal Granule Cells to Context Encoding. Neuron *90*, 101–112.

Dickey, C.A., Loring, J.F., Montgomery, J., Gordon, M.N., Eastman, P.S., and Morgan, D. (2003). Selectively reduced expression of synaptic plasticity-related genes in amyloid precursor protein + presenilin-1 transgenic mice. J. Neurosci. *23*, 5219–5226.

Dobin, A., Davis, C.A., Schlesinger, F., Drenkow, J., Zaleski, C., Jha, S., Batut, P., Chaisson, M., and Gingeras, T.R. (2013). STAR: ultrafast universal RNA-seq aligner. Bioinformatics *29*, 15–21.

Edbauer, D., Neilson, J.R., Foster, K. a., Wang, C.F., Seeburg, D.P., Batterton, M.N., Tada, T., Dolan, B.M., Sharp, P. a., and Sheng, M. (2010). Regulation of Synaptic Structure and Function by FMRP-Associated MicroRNAs miR-125b and miR-132. Neuron *65*, 373–384.

Egeland, M., Guinaudie, C., Du Preez, A., Musaelyan, K., Zunszain, P.A., Fernandes, C., Pariante, C.M., and Thuret, S. (2017). Depletion of adult neurogenesis using the chemotherapy drug temozolomide in mice induces behavioural and biological changes relevant to depression. Transl. Psychiatry *7*, e1101.

Eriksson, P.S., Perfilieva, E., Björk-Eriksson, T., Alborn, A.M., Nordborg, C., Peterson, D.A., and Gage, F.H. (1998). Neurogenesis in the adult human hippocampus. Nat. Med. *4*, 1313–1317.

Espuny-Camacho, I., Michelsen, K.A., Gall, D., Linaro, D., Hasche, A., Bonnefont, J., Bali, C., Orduz, D., Bilheu, A., Herpoel, A., et al. (2013). Pyramidal Neurons Derived from Human Pluripotent Stem Cells Integrate Efficiently into Mouse Brain Circuits In Vivo. Neuron *77*, 440–456.

Espuny-Camacho, I., Arranz, A.M., Fiers, M., Snellinx, A., Ando, K., Munck, S., Bonnefont, J., Lambot,

L., Corthout, N., Omodho, L., et al. (2017). Hallmarks of Alzheimer's Disease in Stem-Cell-Derived Human Neurons Transplanted into Mouse Brain. Neuron *93*, 1066–1081.e8.

El Fatimy, R., Li, S., Chen, Z., Mushannen, T., Gongala, S., Wei, Z., Balu, D.T., Rabinovsky, R., Cantlon, A., Elkhal, A., et al. (2018). MicroRNA-132 provides neuroprotection for tauopathies via multiple signaling pathways. Acta Neuropathol.

Finkel, R.S., Chiriboga, C.A., Vajsar, J., Day, J.W., Montes, J., De Vivo, D.C., Yamashita, M., Rigo, F., Hung, G., Schneider, E., et al. (2016). Treatment of infantile-onset spinal muscular atrophy with nusinersen: a phase 2, open-label, dose-escalation study. Lancet *388*, 3017–3026.

Fortin, D.A., Davare, M.A., Srivastava, T., Brady, J.D., Nygaard, S., Derkach, V.A., and Soderling, T.R. (2010). Long-Term Potentiation-Dependent Spine Enlargement Requires Synaptic Ca2+-Permeable AMPA Receptors Recruited by CaM-Kinase I. J. Neurosci. *30*, 11565–11575.

Fuster-Matanzo, A., Llorens-Martín, M., Hernández, F., and Avila, J. (2013). Role of Neuroinflammation in Adult Neurogenesis and Alzheimer Disease: Therapeutic Approaches. Mediators Inflamm. *2013*, 1–9.

Garthe, A., Behr, J., and Kempermann, G. (2009). Adult-Generated Hippocampal Neurons Allow the Flexible Use of Spatially Precise Learning Strategies. PLoS One *4*, e5464.

Gatt, A., Lee, H., Williams, G., Thuret, S., and Ballard, C. (2019). Expression of neurogenic markers in Alzheimer's disease: a systematic review and metatranscriptional analysis. Neurobiol. Aging *76*, 166–180.

Gonçalves, J.T., Schafer, S.T., and Gage, F.H. (2016). Adult Neurogenesis in the Hippocampus: From Stem Cells to Behavior. Cell *167*, 897–914.

Goold, C.P., and Nicoll, R.A. (2010). Single-Cell Optogenetic Excitation Drives Homeostatic Synaptic Depression. Neuron *68*, 512–528.

Guo, L., Stripay, J.L., Zhang, X., Collage, R.D., Hulver, M., Carchman, E.H., Howell, G.M., Zuckerbraun, B.S., Lee, J.S., and Rosengart, M.R. (2013). CaMKI Regulates AMP Kinase-Dependent, TORC-1-Independent Autophagy during Lipopolysaccharide-Induced Acute Lung Neutrophilic Inflammation. J.

Immunol. *190*, 3620–3628.

Hagihara, H., Toyama, K., Yamasaki, N., and Miyakawa, T. (2009). Dissection of Hippocampal Dentate Gyrus from Adult Mouse. J. Vis. Exp.

Hansen, K.F., Karelina, K., Sakamoto, K., Wayman, G.A., Impey, S., and Obrietan, K. (2013). miRNA-132: a dynamic regulator of cognitive capacity. Brain Struct. Funct. *218*, 817–831.

Hansen, K.F., Sakamoto, K., Aten, S., Snider, K.H., Loeser, J., Hesse, A.M., Page, C.E., Pelz, C., Arthur, J.S.C., Impey, S., et al. (2016). Targeted deletion of miR-132/-212 impairs memory and alters the hippocampal transcriptome. Learn. Mem. *23*, 61–71.

Haughey, N.J., Nath, A., Chan, S.L., Borchard, A.C., Rao, M.S., and Mattson, M.P. (2002). Disruption of neurogenesis by amyloid beta-peptide, and perturbed neural progenitor cell homeostasis, in models of Alzheimer's disease. J. Neurochem. *83*, 1509–1524.

He, N., Jin, W.-L., Lok, K.-H., Wang, Y., Yin, M., and Wang, Z.-J. (2013). Amyloid-β1–42 oligomer accelerates senescence in adult hippocampal neural stem/progenitor cells via formylpeptide receptor 2. Cell Death Dis. *4*, e924–e924.

Hebert, S., Wang, W., Zhu, Q., and Nelson, P. (2013). A Study of Small RNAs from Cerebral Neocortex of Pathology- Verified Alzheimer's Disease, Dementia with Lewy Bodies, Hippocampal Sclerosis, Frontotemporal Lobar Dementia, and Non-Demented Human Controls. J. Alzheimer's Dis. *35*, 335–348.

Hernandez-Rapp, J., Smith, P.Y., Filali, M., Goupil, C., Planel, E., Magill, S.T., Goodman, R.H., and Hébert, S.S. (2015). Memory formation and retention are affected in adult miR-132/212 knockout mice. Behav. Brain Res. *287*, 15–26.

Hochgerner, H., Zeisel, A., Lönnerberg, P., and Linnarsson, S. (2018). Conserved properties of dentate gyrus neurogenesis across postnatal development revealed by single-cell RNA sequencing. Nat. Neurosci. *21*, 290–299.

Jimenez-Mateos, E.M., Bray, I., Sanz-Rodriguez, A., Engel, T., McKiernan, R.C., Mouri, G., Tanaka, K., Sano, T., Saugstad, J. a., Simon, R.P., et al. (2011). MiRNA expression profile after status epilepticus

and hippocampal neuroprotection by targeting miR-132. Am. J. Pathol. *179*, 2519–2532.

Johnston, S.T., Shtrahman, M., Parylak, S., Gonçalves, J.T., and Gage, F.H. (2016). Paradox of pattern separation and adult neurogenesis: A dual role for new neurons balancing memory resolution and robustness. Neurobiol. Learn. Mem. *129*, 60–68.

Kempermann, G., Gage, F.H., Aigner, L., Song, H., Curtis, M.A., Thuret, S., Kuhn, H.G., Jessberger, S., Frankland, P.W., Cameron, H.A., et al. (2018). Human Adult Neurogenesis: Evidence and Remaining Questions. Cell Stem Cell.

Knoth, R., Singec, I., Ditter, M., Pantazis, G., Capetian, P., Meyer, R.P., Horvat, V., Volk, B., and Kempermann, G. (2010). Murine Features of Neurogenesis in the Human Hippocampus across the Lifespan from 0 to 100 Years. PLoS One *5*, e8809.

Kuperstein, I., Broersen, K., Benilova, I., Rozenski, J., Jonckheere, W., Debulpaep, M., Vandersteen, A., Segers-Nolten, I., Van Der Werf, K., Subramaniam, V., et al. (2010). Neurotoxicity of Alzheimer's disease Aβ peptides is induced by small changes in the Aβ42 to Aβ40 ratio. EMBO J. *29*, 3408–3420.

Lau, P., Bossers, K., Janky, R., Salta, E., Frigerio, C.S., Barbash, S., Rothman, R., Sierksma, A.S.R., Thathiah, A., Greenberg, D., et al. (2013). Alteration of the microRNA network during the progression of Alzheimer's disease. EMBO Mol. Med. *5*, 1613–1634.

Lee, I.-S., Jung, K., Kim, I.-S., and Park, K.I. (2013). Amyloid-β oligomers regulate the properties of human neural stem cells through GSK-3β signaling. Exp. Mol. Med. *45*, e60–e60.

Liao, Y., Smyth, G.K., and Shi, W. (2014). featureCounts: an efficient general purpose program for assigning sequence reads to genomic features. Bioinformatics *30*, 923–930.

Liufu, Z., Zhao, Y., Guo, L., Miao, G., Xiao, J., Lyu, Y., Chen, Y., Shi, S., Tang, T., and Wu, C.-I. (2017). Redundant and incoherent regulations of multiple phenotypes suggest microRNAs' role in stability control. Genome Res. *27*, 1665–1673.

Livak, K.J., and Schmittgen, T.D. (2001). Analysis of relative gene expression data using real-time quantitative PCR and the 2(-Delta Delta C(T)) Method. Methods *25*, 402–408.

Lucassen, P.J., Toni, N., Kempermann, G., Frisen, J., Gage, F.H., and Swaab, D.F. (2019). Limits to

human neurogenesis—really? Mol. Psychiatry.

Lucassen, P.J., Fitzsimons, C.P., Salta, E., and Maletic-Savatic, M. (2020). Adult neurogenesis, human after all (again): Classic, optimized, and future approaches. Behav. Brain Res. *381*, 112458.

Luikart, B.W., Bensen, A.L., Washburn, E.K., Perederiy, J. V., Su, K.G., Li, Y., Kernie, S.G., Parada, L.F., and Westbrook, G.L. (2011). MiR-132 mediates the integration of newborn neurons into the adult dentate gyrus. PLoS One *6*.

Magill, S.T., Cambronne, X. a, Luikart, B.W., Lioy, D.T., Leighton, B.H., Westbrook, G.L., Mandel, G., and Goodman, R.H. (2010). microRNA-132 regulates dendritic growth and arborization of newborn neurons in the adult hippocampus. Proc. Natl. Acad. Sci. U. S. A. *107*, 20382–20387.

McAvoy, K.M., Scobie, K.N., Berger, S., Russo, C., Guo, N., Decharatanachart, P., Vega-Ramirez, H., Miake-Lye, S., Whalen, M., Nelson, M., et al. (2016). Modulating Neuronal Competition Dynamics in the Dentate Gyrus to Rejuvenate Aging Memory Circuits. Neuron *91*, 1356–1373.

Mignone, J.L., Kukekov, V., Chiang, A.-S., Steindler, D., and Enikolopov, G. (2004). Neural stem and progenitor cells in nestin-GFP transgenic mice. J. Comp. Neurol. *469*, 311–324.

Moore, M.J., Scheel, T.K.H., Luna, J.M., Park, C.Y., Fak, J.J., Nishiuchi, E., Rice, C.M., and Darnell, R.B. (2015). miRNA–target chimeras reveal miRNA 3′-end pairing as a major determinant of Argonaute target specificity. Nat. Commun. *6*, 8864.

Moreno-Jiménez, E.P., Flor-García, M., Terreros-Roncal, J., Rábano, A., Cafini, F., Pallas-Bazarra, N., Ávila, J., and Llorens-Martín, M. (2019). Adult hippocampal neurogenesis is abundant in neurologically healthy subjects and drops sharply in patients with Alzheimer's disease. Nat. Med. *25*, 554–560.

Mosher, K.I., and Schaffer, D. V. (2018). Influence of hippocampal niche signals on neural stem cell functions during aging. Cell Tissue Res. *371*, 115–124.

Mu, Y., and Gage, F.H. (2011). Adult hippocampal neurogenesis and its role in Alzheimer's disease. Mol. Neurodegener. *6*, 85.

Nakashiba, T., Cushman, J.D., Pelkey, K.A., Renaudineau, S., Buhl, D.L., McHugh, T.J., Barrera, V.R.,

Chittajallu, R., Iwamoto, K.S., McBain, C.J., et al. (2012). Young Dentate Granule Cells Mediate Pattern Separation, whereas Old Granule Cells Facilitate Pattern Completion. Cell *149*, 188–201.

Naskar, D., Maiti, G., Chakraborty, A., Roy, A., Chattopadhyay, D., and Sen, M. (2014). Wnt5a-Rac1-NF-κB homeostatic circuitry sustains innate immune functions in macrophages. J. Immunol. *192*, 4386–4397.

Niibori, Y., Yu, T.-S., Epp, J.R., Akers, K.G., Josselyn, S.A., and Frankland, P.W. (2012). Suppression of adult neurogenesis impairs population coding of similar contexts in hippocampal CA3 region. Nat. Commun. *3*, 1253.

Overk, C.R., and Masliah, E. (2014). Toward a unified therapeutics approach targeting putative amyloid- oligomer receptors. Proc. Natl. Acad. Sci. *111*, 13680–13681.

Paredes, M.F., Sorrells, S.F., Cebrian-Silla, A., Sandoval, K., Qi, D., Kelley, K.W., James, D., Mayer, S., Chang, J., Auguste, K.I., et al. (2018). Does Adult Neurogenesis Persist in the Human Hippocampus? Cell Stem Cell *23*, 780–781.

Patrick, E., Rajagopal, S., Wong, H.-K.A., McCabe, C., Xu, J., Tang, A., Imboywa, S.H., Schneider, J.A., Pochet, N., Krichevsky, A.M., et al. (2017). Dissecting the role of non-coding RNAs in the accumulation of amyloid and tau neuropathologies in Alzheimer's disease. Mol. Neurodegener. *12*, 51.

Petersen, R.C., Doody, R., Kurz, A., Mohs, R.C., Morris, J.C., Rabins, P. V, Ritchie, K., Rossor, M., Thal, L., and Winblad, B. (2001). Current concepts in mild cognitive impairment. Arch. Neurol. *58*, 1985–1992.

Picelli, S., Björklund, Å.K., Faridani, O.R., Sagasser, S., Winberg, G., and Sandberg, R. (2013). Smart-seq2 for sensitive full-length transcriptome profiling in single cells. Nat. Methods *10*, 1096–1098.

Pichler, S., Gu, W., Hartl, D., Gasparoni, G., Leidinger, P., Keller, A., Meese, E., Mayhaus, M., Hampel, H., and Riemenschneider, M. (2017). The miRNome of Alzheimer's disease: consistent downregulation of the miR-132/212 cluster. Neurobiol. Aging *50*, 167.e1-167.e10.

Pillat, M.M., Lameu, C., Trujillo, C.A., Glaser, T., Cappellari, A.R., Negraes, P.D., Battastini, A.M.O.,

Schwindt, T.T., Muotri, A.R., and Ulrich, H. (2016). Bradykinin promotes neuron-generating division of neural progenitor cells through ERK activation. J. Cell Sci. *129*, 3437–3448.

van Praag, H., Kempermann, G., and Gage, F.H. (1999). Running increases cell proliferation and neurogenesis in the adult mouse dentate gyrus. Nat. Neurosci. *2*, 266–270.

van Praag, H., Schinder, A.F., Christie, B.R., Toni, N., Palmer, T.D., and Gage, F.H. (2002). Functional neurogenesis in the adult hippocampus. Nature *415*, 1030–1034.

Radde, R., Bolmont, T., Kaeser, S.A., Coomaraswamy, J., Lindau, D., Stoltze, L., Calhoun, M.E., Jäggi, F., Wolburg, H., Gengler, S., et al. (2006). Abeta42-driven cerebral amyloidosis in transgenic mice reveals early and robust pathology. EMBO Rep. *7*, 940–946.

Riascos, D., Nicholas, A., Samaeekia, R., Yukhananov, R., Mesulam, M.-M., Bigio, E.H., Weintraub, S., Guo, L., and Geula, C. (2014). Alterations of Ca^{2+}-responsive proteins within cholinergic neurons in aging and Alzheimer's disease. Neurobiol. Aging *35*, 1325–1333.

Rueden, C.T., Schindelin, J., Hiner, M.C., DeZonia, B.E., Walter, A.E., Arena, E.T., and Eliceiri, K.W. (2017). ImageJ2: ImageJ for the next generation of scientific image data. BMC Bioinformatics *18*, 529.

Sahay, A., Scobie, K.N., Hill, A.S., O'Carroll, C.M., Kheirbek, M.A., Burghardt, N.S., Fenton, A.A., Dranovsky, A., and Hen, R. (2011). Increasing adult hippocampal neurogenesis is sufficient to improve pattern separation. Nature *472*, 466–470.

Saito, T., Matsuba, Y., Mihira, N., Takano, J., Nilsson, P., Itohara, S., Iwata, N., and Saido, T.C. (2014). Single App knock-in mouse models of Alzheimer's disease. Nat. Neurosci. *17*, 661–663.

Salta, E., and De Strooper, B. (2017). microRNA-132: a key noncoding RNA operating in the cellular phase of Alzheimer's disease. FASEB J. *31*, 424–433.

Salta, E., Lau, P., Sala Frigerio, C., Coolen, M., Bally-Cuif, L., and De Strooper, B. (2014). A self-organizing miR-132/Ctbp2 circuit regulates bimodal notch signals and glial progenitor fate choice during spinal cord maturation. Dev. Cell *30*, 423–436.

Salta, E., Sierksma, A., Vanden Eynden, E., and De Strooper, B. (2016). miR-132 loss de-represses ITPKB and aggravates amyloid and TAU pathology in Alzheimer's brain. EMBO Mol. Med. *8*, 1005–

1018.

Serneels, L., Van Biervliet, J., Craessaerts, K., Dejaegere, T., Horré, K., Van Houtvin, T., Esselmann, H., Paul, S., Schäfer, M.K., Berezovska, O., et al. (2009). gamma-Secretase heterogeneity in the Aph1 subunit: relevance for Alzheimer's disease. Science *324*, 639–642.

Shi, Y., Kirwan, P., and Livesey, F.J. (2012). Directed differentiation of human pluripotent stem cells to cerebral cortex neurons and neural networks. Nat. Protoc. *7*, 1836–1846.

Shin, J., Berg, D.A., Zhu, Y., Shin, J.Y., Song, J., Bonaguidi, M.A., Enikolopov, G., Nauen, D.W., Christian, K.M., Ming, G., et al. (2015). Single-Cell RNA-Seq with Waterfall Reveals Molecular Cascades underlying Adult Neurogenesis. Cell Stem Cell *17*, 360–372.

Smith, P.Y., Hernandez-Rapp, J., Jolivette, F., Lecours, C., Bisht, K., Goupil, C., Dorval, V., Parsi, S., Morin, F., Planel, E., et al. (2015). miR-132/212 deficiency impairs tau metabolism and promotes pathological aggregation in vivo. Hum. Mol. Genet. *24*, 6721–6735.

Snyder, J.S. (2019). Recalibrating the Relevance of Adult Neurogenesis. Trends Neurosci.

Sorrells, S.F., Paredes, M.F., Cebrian-Silla, A., Sandoval, K., Qi, D., Kelley, K.W., James, D., Mayer, S., Chang, J., Auguste, K.I., et al. (2018). Human hippocampal neurogenesis drops sharply in children to undetectable levels in adults. Nature.

Spalding, K.L., Bergmann, O., Alkass, K., Bernard, S., Salehpour, M., Huttner, H.B., Boström, E., Westerlund, I., Vial, C., Buchholz, B.A., et al. (2013). Dynamics of hippocampal neurogenesis in adult humans. Cell *153*, 1219–1227.

Suárez-Pereira, I., Canals, S., and Carrión, Á.M. (2015). Adult newborn neurons are involved in learning acquisition and long-term memory formation: The distinct demands on temporal neurogenesis of different cognitive tasks. Hippocampus *25*, 51–61.

Suh, H., Zhou, Q.-G., Fernandez-Carasa, I., Clemenson, G.D., Pons-Espinal, M., Ro, E.J., Marti, M., Raya, A., Gage, F.H., and Consiglio, A. (2018). Long-Term Labeling of Hippocampal Neural Stem Cells by a Lentiviral Vector. Front. Mol. Neurosci. *11*, 415.

Susaki, E.A., Tainaka, K., Perrin, D., Yukinaga, H., Kuno, A., and Ueda, H.R. (2015). Advanced CUBIC

protocols for whole-brain and whole-body clearing and imaging. Nat. Protoc. *10*, 1709–1727.

Tartt, A.N., Fulmore, C.A., Liu, Y., Rosoklija, G.B., Dwork, A.J., Arango, V., Hen, R., Mann, J.J., and Boldrini, M. (2018). Considerations for Assessing the Extent of Hippocampal Neurogenesis in the Adult and Aging Human Brain. Cell Stem Cell *23*, 782–783.

Theus, M.H., Ricard, J., Bethea, J.R., and Liebl, D.J. (2010). EphB3 limits the expansion of neural progenitor cells in the subventricular zone by regulating p53 during homeostasis and following traumatic brain injury. Stem Cells *28*, 1231–1242.

Tobin, M.K., Musaraca, K., Disouky, A., Shetti, A., Bheri, A., Honer, W.G., Kim, N., Dawe, R.J., Bennett, D.A., Arfanakis, K., et al. (2019). Human Hippocampal Neurogenesis Persists in Aged Adults and Alzheimer's Disease Patients. Cell Stem Cell.

Toda, T., Parylak, S.L., Linker, S.B., and Gage, F.H. (2018). The role of adult hippocampal neurogenesis in brain health and disease. Mol. Psychiatry.

Trinchero, M.F., Buttner, K.A., Sulkes Cuevas, J.N., Temprana, S.G., Fontanet, P.A., Monzón-Salinas, M.C., Ledda, F., Paratcha, G., and Schinder, A.F. (2017). High Plasticity of New Granule Cells in the Aging Hippocampus. Cell Rep. *21*, 1129–1139.

Vadodaria, K.C., Brakebusch, C., Suter, U., and Jessberger, S. (2013). Stage-specific functions of the small Rho GTPases Cdc42 and Rac1 for adult hippocampal neurogenesis. J. Neurosci. *33*, 1179–1189.

Villeda, S.A., Luo, J., Mosher, K.I., Zou, B., Britschgi, M., Bieri, G., Stan, T.M., Fainberg, N., Ding, Z., Eggel, A., et al. (2011). The ageing systemic milieu negatively regulates neurogenesis and cognitive function. Nature *477*, 90–94.

Wang, Y., Veremeyko, T., Wong, A.H.-K., El Fatimy, R., Wei, Z., Cai, W., and Krichevsky, A.M. (2017). Downregulation of miR-132/212 impairs S-nitrosylation balance and induces tau phosphorylation in Alzheimer's disease. Neurobiol. Aging *51*, 156–166.

Wesnes, K.A., Annas, P., Basun, H., Edgar, C., and Blennow, K. (2014). Performance on a pattern separation task by Alzheimer's patients shows possible links between disrupted dentate gyrus activity and apolipoprotein E ∈4 status and cerebrospinal fluid amyloid-β42 levels. Alzheimers. Res.

Ther. *6*, 20.

Wong, H.K.A., Veremeyko, T., Patel, N., Lemere, C.A., Walsh, D.M., Esau, C., Vanderburg, C., and Krichevsky, A.M. (2013). De-repression of FOXO3a death axis by microRNA-132 and -212 causes neuronal apoptosis in Alzheimer's disease. Hum. Mol. Genet. *22*, 3077–3092.

Yang, Y.-T., Wang, C.-L., and Van Aelst, L. (2012). DOCK7 interacts with TACC3 to regulate interkinetic nuclear migration and cortical neurogenesis. Nat. Neurosci. *15*, 1201–1210.

Yassa, M.A., Stark, S.M., Bakker, A., Albert, M.S., Gallagher, M., and Stark, C.E.L. (2010). High-resolution structural and functional MRI of hippocampal CA3 and dentate gyrus in patients with amnestic Mild Cognitive Impairment. Neuroimage *51*, 1242–1252.

Yuniati, L., Scheijen, B., van der Meer, L.T., and van Leeuwen, F.N. (2018). Tumor suppressors BTG1 and BTG2: Beyond growth control. J. Cell. Physiol.

Zeisel, A., Hochgerner, H., Lönnerberg, P., Johnsson, A., Memic, F., van der Zwan, J., Häring, M., Braun, E., Borm, L.E., La Manno, G., et al. (2018). Molecular Architecture of the Mouse Nervous System. Cell *174*, 999–1014.e22.

Zhao, C. (2006). Distinct Morphological Stages of Dentate Granule Neuron Maturation in the Adult Mouse Hippocampus. J. Neurosci. *26*, 3–11.

Zhao, C., Teng, E.M., Summers, R.G., Ming, G.-L., and Gage, F.H. (2006). Distinct morphological stages of dentate granule neuron maturation in the adult mouse hippocampus. J. Neurosci. *26*, 3–11.

Zhu, Q. Bin, Unmehopa, U., Bossers, K., Hu, Y.T., Verwer, R., Balesar, R., Zhao, J., Bao, A.M., and Swaab, D. (2016). MicroRNA-132 and early growth response-1 in nucleus basalis of Meynert during the course of Alzheimer's disease. Brain *139*, 908–921.

Figure legends

Figure 1. Adult neurogenesis is impaired by AD pathology and is associated with miR-132 levels. A. Schematic representation of the main fate transitions during adult hippocampal neurogenesis in the dentate gyrus (DG), including radial glia (RG)-like neural stem cells (NSCs), neuronal precursor cells (NPCs), neuroblasts, immature and mature neurons, as indicated by the expression pattern of distinct molecular markers. B. Semi-quantitative real-time PCR of miR-132 levels in the dentate gyrus of C57Bl/6, *APP/PS1* and *App*$^{NL\text{-}G\text{-}F}$ mice at 3, 6, 9 and 12 months of age. N=3-6 mice per time point. C. Quantification of experiment illustrated in panel E. BrdU^{+}-cells in the subgranular zone of the dentate gyrus in C57Bl/6, *APP/PS1* and *App*$^{NL\text{-}G\text{-}F}$ control (Sedentary) mice or mice exposed to voluntary running for 1 month (Run) at 3, 6 and 9 months of age. N=4-6 mice per group. D. Semi-quantitative real-time PCR of miR-132 levels in the dentate gyrus of C57Bl/6, *APP/PS1* and *App*$^{NL\text{-}G\text{-}F}$ sedentary control or running mice at 3, 6 and 9 months of age. N=4-6 mice per group. E. BrdU^{+}-proliferating neuronal progenitors in C57Bl/6, *APP/PS1* and *App*$^{NL\text{-}G\text{-}F}$ sedentary control or running mice at 3, 6 and 9 months of age. Scale bars, 50 µm. Values are presented as mean ± SEM. In (B), two-way ANOVA with Tukey's *post hoc* test for multiple comparisons were employed, while in (C, D), Student's t-test was used. **See also Figure S1 and Table S1.**

Figure 2. miR-132 in the adult hippocampal neurogenic niche. A, B. miR-132 *in situ* hybridization coupled to GFP and Ki-67 (A) or GFP and doublecortin (DCX) (B) immunolabeling in the dentate gyrus of 3-month-old Nestin:GFP mice. Lower panels show magnified views of the cells in the regions indicated by dashed rectangles in upper panels. Dashed outlines in lower panels indicate cellular margins. Scale bars, 50 µm (upper panels); 10 µm (lower panels). C. Semi-quantitative real-time PCR of miR-132 levels in GFP^{+} or GFP^{-} populations isolated by FACS from the dentate gyrus of Nestin:GFP mice at 1.5, 3, 6, 9 and 12 months of age. N=6-8 mice per time point. D, E. Semi-quantitative real-time PCR of miR-132 levels in GFP^{+} (D) or GFP^{-} (E) populations sorted from the dentate gyrus of sedentary

control or running Nestin:GFP mice at 3 months of age. N=6-8 mice per group. F. Semi-quantitative real-time PCR of miR-132 levels in GFP^+ or GFP^- populations sorted from the dentate gyrus of Nestin-NLGF mice at 1.5, 3, 6, 9 and 12 months of age. N=3-5 mice per time point. Values are presented as mean ± SEM. In (C, F), two-way ANOVA with Tukey's *post hoc* test for multiple comparisons were applied, while in (D, E), Student's t-test was used. **See also Figure S2 and Table S4.**

Figure 3. miR-132 is required for adult neurogenesis. A. Quantification of $BrdU^+$-cells in the dentate gyrus of control- or AntagomiR-132 (Ant-132) -injected, sedentary or running C57Bl/6 mice at 9 months of age. N=6-9 mice per group. B-D. Quantification of Ki-67^+- (B), Nestin:GFP^+- (C) and DCX^+-cells (D) in the dentate gyrus of control- or Ant-132-injected, sedentary or running Nestin:GFP mice at 3 months of age. N=4-6 mice per group. E. $BrdU^+$-proliferating neuronal progenitors in the dentate gyrus of scramble- or Ant-132-injected, sedentary or running C57Bl/6 mice at 9 months of age. Arrowheads indicate $BrdU^+$-cells. Scale bars, 50 µm. F. Ki-67^+-proliferating progenitors and DCX^+-immature neurons in control- or Ant-132-injected, sedentary or running Nestin:GFP mice at 3 months of age. Arrowheads indicate Ki-67^+-amplifying progenitors. Scale bars, 50 µm. G. Schematic of mouse brain indicating the area of sectioning (dashed lines) used for tissue clearing. H. Coronal mouse brain section at P56, position 293, showing hippocampal structure. Image adapted from Allen Brain Atlas (http://mouse.brain-map.org/experiment/thumbnails/100048576?image_type=atlas). I. Cleared coronal brain section. J. Quantification of GFP^+-cells in the subgranular layer of the dentate gyrus in running scramble- or Ant-132-injected 3-month-old Nestin:GFP mice. N=10 mice per group; 2 hemispheric dentate gyri per mouse. K, L. 3D reconstruction and image processing for whole-mount GFP^+-cell counting in scramble- (K) or Ant-132- (L) injected mice upon running. Green, GFP^+-cells; dark blue, reconstructed dentate gyrus surface; purple, GFP^+-cells lining the dentate gyrus used for quantification; light blue, GFP^+-cells away from dentate gyrus. Scale bar, 300 µm. Values are presented

as mean ± SEM. Two-way ANOVA with Tukey's *post hoc* test for multiple comparisons were employed in (A-D) and Student's t-test in (J). **See also Figure S3.**

Figure 4. miR-132 regulatory effects in human neural stem cells. A. Schematic representation of the protocol used for neural induction of human embryonic pluripotent stem cells (EPSCs). DIV, days *in vitro*. B, C. Semi-quantitative real-time PCR of miR-132 (B) and tubulin (*TUBB3*) (C) levels in EPSCs (Day -2), NPCs (Day 29) and mature neurons (Day 60). N=3 independent experiments. D. Schematic diagram of the protocol used for neural differentiation of cultured immortalized human mesencephalic neuronal progenitors. NSCs/NPCs, neural stem cells/neuronal progenitor cells; aNPCs, amplifying neuronal progenitor cells; DPD, days post differentiation; E. Semi-quantitative real-time PCR of miR-132 and *TUBB3* upon induction of differentiation (Diff) in human neuronal progenitors. N=3 independent experiments. F, G. Semi-quantitative real-time PCR of *TUBB3* following miR-132 overexpression (miR-132) without induction of differentiation (F) or miR-132 knockdown (miR-132 Inh) upon induction of differentiation at 3 days post differentiation (G). N=3 independent experiments per condition. H. Schematic diagram of the protocol used for neural differentiation of cultured immortalized human hippocampal neuronal progenitors. I, J. Semi-quantitative real-time PCR of miR-132 and *TUBB3* following miR-132 overexpression (miR-132) without induction of differentiation (I) or miR-132 knockdown (miR-132 Inh) upon induction of differentiation at 3 days post differentiation (J). N=3 independent experiments per condition. K, L. Semi-quantitative real-time PCR of the proliferation marker *MKI67* (coding for Ki-67) and miR-132 in embryonic pluripotent stem cell-derived primary human neuronal precursor cells (NPC) (K) or an established human hippocampal neural precursor (hNPC) line (HPC0A07/03CI) (L) upon treatment with $A\beta_{1-42}$ oligomers and a scramble control peptide (K) or incubation in AD and control serum (L). N=6 biological replicates in (K); 23 (ND) and 17 (AD) in (L). Values are presented as mean ± SEM. For data analysis, one-way ANOVA with Tukey's *post hoc* test

for multiple comparisons were applied in (B, C, E), while Student's t-test was used in (F, G, I-L)). **See also Figure S4.**

Figure 5. miR-132 overexpression ameliorates adult neurogenesis deficits in AD mouse hippocampus. A. Immunolabeling of $BrdU^+$-, Ki-67^+- and DCX^+-cells in the dentate gyrus of control- (Ctr) or miR-132 (miR-132)-injected, sedentary or running *APP/PS1* mice at 9 months of age. Scale bar, 50 µm. B-D. Quantification of $BrdU^+$- (B), Ki-67^+- (C) and DCX^+-cells (D) in the dentate gyrus of control- (Ctr) or miR-132 (miR-132)-injected, sedentary or running *APP/PS1* mice at 9 months of age. N=6-10 mice per group. E. Immunolabeling of $BrdU^+$-, Ki-67^+- and DCX^+-cells in the dentate gyrus of control- (Ctr) or miR-132 (miR-132)-injected, sedentary or running $App^{NL\text{-}G\text{-}F}$ mice at 9 months of age. Scale bar, 50 µm. F-H. Quantification of $BrdU^+$- (F), Ki-67^+- (G) and DCX^+-cells (H) in the dentate gyrus of control- (Ctr) or miR-132 (miR-132)-injected, sedentary or running $App^{NL\text{-}G\text{-}F}$ mice at 9 months of age. N=6-10 mice per group. I. Semi-quantitative real-time PCR of *Pax6*, *Mki67* and *Dcx* levels in GFP^+-cells sorted from the dentate gyrus of Nestin:GFP mice at 3 months of age upon control- or miR-132-injection. N=5-6 mice per group. Values are presented as mean ± SEM. For data analysis, two-way ANOVA with Tukey's *post hoc* test for multiple comparisons were applied in (B-D, F-H), while Student's t-test was used in (I). **See also Figure S5.**

Figure 6. Cell-autonomous effects of miR-132 in adult-born neurons in AD mouse brain. A. Schematic diagram of the experimental design. Lentiviral and retroviral vectors were used for stereotactic injections into the dentate gyrus of 9-month old $App^{NL\text{-}G\text{-}F}$ mice. Animals were housed under sedentary or running conditions and were euthanized 4 weeks post injection. B, C. Semi-quantitative real-time PCR of miR-132 in FACsorted $mCHERRY^+$-cells (B) or dentate gyri (C) upon miR-132 overexpression compared to the respective control vector injections. N=3 mice per group. D, E. Immunolabeling of $mCHERRY^+$- (D) or GFP^+- (E) 4-week old neurons upon lentiviral (D) or retroviral (E) miR-132

overexpression in *App*$^{NL-G-F}$ animals, under sedentary or running conditions. F, G. Imaging and quantification of dendritic length and complexity in 4-week old neurons upon miR-132 lentiviral (F) or retroviral (G) overexpression in *App*$^{NL-G-F}$ animals, under sedentary or running conditions. N=3 mice per group; 4-6 cells per mouse. H, I. Imaging of dendritic spines in 4-week old neurons upon miR-132 lentiviral (H) or retroviral (I) overexpression in *App*$^{NL-G-F}$ animals, under sedentary or running conditions. J, K. Quantification of spine density in 4-week old neurons upon miR-132 lentiviral (H) or retroviral (I) overexpression in *App*$^{NL-G-F}$ animals, under sedentary or running conditions. N=3 mice per group; 1 dendrite per cell; 4-6 cells per mouse. Scale bars, 50 µm (D, E); 10 µm (H, I). Values are presented as mean ± SEM. For data analysis, two-way ANOVA with Tukey's *post hoc* test for multiple comparisons were applied in (F, G, J, K), while Student's t-test was used in (B, C).

Figure 7. Single-cell approach to identify miR-132 targets in AHN. A. Schematic diagram of the experimental workflow used to isolate and analyze adult Nestin:GFP^{+} niche cells from the mouse dentate gyrus upon miR-132 overexpression. B. Unsupervised hierarchical clustering of dataset, cell type mapping and cell type-specific marker expression. Cell numbers per cluster are indicated in parentheses. C. Semi-quantitative real-time PCR assessment of predicted miR-132 target transcripts in the human RenCell line upon transfection with miR-132 mimic or a control oligonucleotide. N=3 independent experiments. RGL, radial glia-like cells; NPC, neuronal intermediate progenitor cells; OPC, oligodendrocyte precursors; MFOL, myelin-forming oligodendrocytes; In C, two-way ANOVA with Tukey's *post hoc* test for multiple comparisons were used. Dashed line indicates mean fold change of control samples set at 1. Values are presented as mean ± SEM. **See also Figure S6 and Tables S5, S6.**

Figure 8. miR-132 overexpression restores memory deficits in AD mice. A. Latency time (indicated in seconds, s) in passive avoidance test upon control or miR-132 injections in wild-type and AD mice. B. Schematic diagram of pattern separation test. Mice were fear-conditioned for 3 days in shock-receiving

context A, and subsequently tested for their ability to discriminate between similar contexts A and B, and between different contexts A and C. C. Percentage of time spent freezing by control (Ctr)- or miR-132 (miR-132)-injected 9-month-old wild-type (C57Bl/6) or *App*$^{NL-G-F}$ mice during days 1-3 of fear acquisition. D, E. Percentage of time spent freezing in contexts A and C (D) or A and B (E) during days 4-5 of generalization testing. N=12-15 mice per group. F. Schematic diagram of passive avoidance test in 9-month-old *App*$^{NL-G-F}$ mice employing saline or temozolomide (TMZ) intraperitoneal (i.p.) injections and control (Ctr) or miR-132 (miR-132) intracerebroventricular injections. G. Ki-67 immunolabeling in the dentate gyrus of saline or TMZ-, Ctr- or miR-132-injected *App*$^{NL-G-F}$ mice after passive avoidance test completion. H. Quantification of Ki-67^{+}-cells upon saline or TMZ injections in Ctr- or miR-132-injected *App*$^{NL-G-F}$ mice. N=11-13 mice per group. Scale bar, 50 µm. I. Latency time in passive avoidance test in saline or TMZ-injected, Ctr- or miR-132-injected *App*$^{NL-G-F}$ mice. Values are presented as mean ± SEM. N=11-13 mice per group. For data analysis, two-way ANOVA with Tukey's *post hoc* test for multiple comparisons were employed. **See also Figure S5.**

STAR Methods

Animals

The wild-type mice we used were C57BL/6. The AD mouse models used in the study were the *APP/PS1* and *App*$^{NL-G-F}$ strains. The first mouse model co-expresses human-mutated APP^{Swe} (KM670/671NL APP) and human mutated presenilin 1 (L166P). These mice [Tg(Thy1-APPSw, Thy1-PSEN1*L166P) 21Jckr] typically show amyloid deposition in the hippocampus at 3–4 months and cognitive impairment at 7–8 months of age (Radde et al., 2006; Serneels et al., 2009). *App*$^{NL-G-F}$ mice are a more recently established App knock-in model that expresses the APP KM670/671NL (Swedish), APP I716F (Iberian), APP E693G (Arctic) mutations. Similarly to the *APP/PS1* mice, *App*$^{NL-G-F}$ animals develop plaques around the age of 3 months and behavioral deficits from 6 months onwards (Saito et al., 2014). For neural stem cell and neuronal progenitor cell visualization *in vivo* and cell isolation from the adult dentate

gyrus, the previously characterized Nestin:GFP mice were used (Mignone et al., 2004). For Nestin:GFP^{+}-niche cell sorting from the AD dentate gyrus, Nestin:GFP mice were crossed to *App*$^{NL\text{-}G\text{-}F}$ animals (Nestin-NLGF). All animal experiments were approved by the ethical committees of KU Leuven and UZ Leuven (LA1210596).

Human samples

The clinical and histopathological information regarding the human hippocampal samples used in the study is summarized in Table S1. Information on collection and processing of the serum samples is provided in Table S4. All experimental procedures with human samples were approved by the ethical committees of KU Leuven, UZ Leuven (S59654) and the University of Gothenburg.

Intracerebroventricular (ICV) injections

The intracerebroventricular injections were performed as previously described (Jimenez-Mateos et al., 2011) using the following stereotactic coordinates: AP-0.1 mm, ML-1.0 mm, and DV-3.0 mm (from the skull). For miR-132 knockdown, 2 month-old Nestin:GFP or 8 month-old C57Bl/6 mice were infused with 2 µl of miR-132 antagomiR (locked nucleic acid (LNA)-, 3'-cholesterol-modified oligonucleotide) (Exiqon, Qiagen, Denmark) at 0.33 nmole/µl in artificial cerebrospinal fluid (aCSF) (Harvard Apparatus, USA). Control mice received a scrambled LNA oligonucleotide in aCSF. Mice were exposed to voluntary running one week post operation. Analysis of antagomiR-132-injected animals was performed at 3 and 9 months of age, respectively (after 4 weeks of voluntary running). For miR-132 overexpression, 2 month-old Nestin:GFP or 8 month-old *App*$^{NL\text{-}G\text{-}F}$ and *APP/PS1* mice received either a miR-132 mimic or a negative control oligonucleotide (Dharmacon, Horizon Discovery, Belgium) in a 3 µl mix with lipofectamine 2000 (at a 1:1 volume ratio) (Thermo Fischer Scientific, Belgium). Injections of 150 pmol oligo each were performed once a week for 5 weeks in total. One week after the first injection, mice were exposed to voluntary running for a total of 4 weeks. Analysis of miR-132 mimic-injected animals

was carried out at 9 months of age. Randomization of injectates was employed for all injection sessions, and animals were randomly allocated to each treatment.

Viral vector injections into the dentate gyrus

Male and female 9-month old *App*$^{NL-G-F}$ mice were housed in standard (sedentary) conditions or with a running wheel 1 week prior to surgery. For miR-132 overexpression in adult neural stem cells or progeny, a lentiviral Puro:mPGK:mCHERRY backbone vector (Suh et al., 2018) or a retroviral CAG:GFP (Zhao et al., 2006) construct were used, respectively, harboring a miR-132 hairpin sequence (VectorBuilder, Germany). Hairpin constructs corresponding to cel-miR-67 were used as negative controls. For stereotactic injections, the viruses were infused (lentivirus: 10^9 TU/ml; 2 µl at 0.5 µl min^{-1}; retrovirus: 10^8 TU/ml; 5 µl at 0.5 µl min^{-1}) into the hemispheric right dentate gyrus (anteroposterior: -2.1 mm from Bregma; mediolateral: 1.9 mm; dorsoventral: 2.2 mm) (van Praag et al., 2002). Mice were kept under sedentary or running conditions and were sacrificed 4 weeks post injection.

Induction of AHN via voluntary running

Mice were housed individually in standard rat cages (45 cm x 20 cm x 20 cm) and divided into sedentary or running groups. Runners had unlimited access to a running wheel in their cage for 30 days. Running distance (km) was monitored electronically (MAFAC, France). No differences in running velocity or distance were observed between wild-type and AD animals.

5-Bromo-2'-deoxyuridine (BrdU) injections

BrdU (Sigma-Aldrich, Belgium) was dissolved in 0.9% NaCl at a concentration of 10 mg/ml and was filtered (0.2 µm) under sterile conditions. Mice were pulsed with a single i.p. injection of BrdU (50 mg/kg of body weight) daily for 3 days (at the end of the running period). 24 h after the last BrdU injection they were perfused with 4% paraformaldehyde (PFA) and processed for BrdU immunostaining to identify proliferating neuronal progenitors.

Immunofluorescence in mouse brain sections and cultured cells

For coronal brain sections (16 µm-thick cryosections for VGlut1/PSD95 stainings; 20 µm-thick cryosections for BrdU staining; 40 µm-thick vibratome-prepared sections for Nestin:GFP, Ki-67, DCX staining), tissue was initially permeabilized in 1% (v/v) TritonX-100 (cryosections were first post-fixed in 4% PFA for BrdU and in acetone/methanol for VGlut1/PSD95) and then blocked in 1% (v/v) TritonX-100, 10% (v/v) normal goat serum in PBS for 2 h at room temperature. Primary antibody incubation was carried out in 0.3% (v/v) TritonX-100, 3% (v/v) normal goat serum overnight at 4°C followed by incubation in secondary antibody for 2 h at room temperature. Finally, sections were incubated in DAPI (Sigma-Aldrich, Belgium) and mounted in Mowiol. For immunofluorescent labeling in cells cultured on coverslips, samples were initially permeabilized like before and then incubated in blocking solution (1.5% (v/v) normal donkey serum, 0.2% (v/v) TritonX-100 in PBS) for 1 h at room temperature. Primary and secondary antibody incubation was carried out in blocking solution at 4°C overnight and for 2 h at room temperature, respectively. Finally, cells were stained with DAPI and mounted as described earlier. All the antibodies used for immunolabeling of brain tissue and cultured cells are listed in Table S2.

Immunostaining of human hippocampal sections

An automated staining protocol (Bond Polymer Refine Detection Protocol, Leica Microsystems, Belgium) was followed using a Leica Autostainer (Leica Microsystems, Belgium). Briefly, following dewaxing and rehydration, 5 µm-thick formalin-fixed, paraffin-embedded hippocampal sections were first blocked in 3-4% (v/v) H_2O_2 and then incubated sequentially with the primary antibody for 30 min, with anti-rabbit poly-HRP IgGs, DAB (3,3'-Diaminobenzidine tetrahydrochloride hydrate) and hematoxylin. In the case of double stainings, the second primary antibody was added to the sections after hematoxylin staining and was followed by incubation in an AP-conjugated antibody and in Bond Polymer Refine Red Detection reagent (Leica Microsystems, Belgium). Finally, the sections were

dehydrated and mounted on a Leica automated Coverslipper (Leica Microsystems, Belgium). The antibodies used for immunostaining of human brain samples are listed in Table S2.

Tissue clearing

For brain clearing, the CUBIC protocol (Susaki et al., 2015) was adapted. Briefly, two 1 mm-thick coronal brain sections (Interaural: 1.68/0.88 mm, Bregma: -2.12/-2.92 mm) from 4% PFA-perfused brains were initially immersed in 12.5% (w/w) urea, 12.5% (w/w) quadrol and 7.5% (w/w) TritonX-100 for 6 h at 37°C for lipid removal. Subsequently, samples were incubated in 25% (w/w) urea, 25% (w/w) quadrol, and 15% (w/w) TritonX-100 for 24 h at 37°C and the clearing reagent was refreshed after 48 h. The clearing procedure was stopped with washes in 0.01% (w/v) sodium azide in PBS. Refractive index matching was achieved by incubating the sections in 25% (w/w) sucrose, 12.5% (w/w) urea, 5% (w/w) triethanolamine and 0.05% (v/v) TritonX-100 for 24 h at 37°C and then in 50% (w/w) sucrose, 25% (w/w) urea, 10% (w/w) triethanolamine and 0.1% (v/v) TritonX-100 for 48 h with refreshing the solution every 24 h.

Fluorescence *in situ* hybridization (FISH)

40 µm-thick vibratome coronal brain sections were post-fixed in 4% PFA for 15 min and then acetylated in a hydrochloric acid, triethylamine, acetic anhydride solution for 1 min in the dark. Following prehybridization in hybridization buffer (50% formamide, 5x saline-sodium citrate (SSC), 500 µg/ml yeast t-RNA, 1x Denhardt's solution) at 60°C for 1 h, samples were hybridized with 42 nM of miR-132 or scramble probe (Ribotask, Denmark) at 70°C overnight. After sequential washes in 0.2x, 0.5x, 2x SSC buffer and brief incubation in 3% H_2O_2, blocking was performed in 0.5% Blocking Reagent (blocking solution) (Roche Diagnostics, Belgium) for 1 h at room temperature. Finally, sections were probed with an antifluorescein HRP-conjugated antibody (Roche Diagnostics, Belgium) in blocking solution for 1 h and signals were developed in TSA Plus Fluorescein reagent (Perkin Elmer, USA). For subsequent immunofluorescent labeling, the sections were processed as described earlier.

Image acquisition, processing and analysis

For the PCNA staining in human samples, one hippocampal section per case was screened using a widefield Zeiss Axioplan 2 (Zeiss, Belgium). $PCNA^+$-nuclei at the subgranular layer of the dentate gyrus within an area that included in total 1000 hematoxylin-stained nuclei were encountered for quantification. Cells with cytoplasmic $PCNA^+$-signal were excluded from the analysis, as these may include IBA^+-proliferating microglia (see Figure S1). The average of the cell counts in the non-demented control cohort was used for the normalization of all the samples.

For immunolabelled mouse brain sections and cultured cells, images (z-stacks) were acquired using a Nikon A1R Eclipse Ti confocal microscope (Nikon, Belgium), unless differently stated. The FIJI software (Rueden et al., 2017) was employed for image processing and quantification. For BrdU immunostaining in cryosections, three sections per sample were used with 200 µm distance between each two sections. The number of $BrdU^+$-cells in the subgranular zone of the dentate gyrus was normalized to the total length of the dentate for each section ($BrdU^+$-cells divided by dentate gyrus length). Average values for each sample were calculated by averaging the normalized values of the three sections per sample. For Nestin:GFP, Ki-67 and DCX immunostaining in vibratome-prepared sections, 9-12 sections (with 40 µm distance between each two sections) per sample were used for quantification. $Ki\text{-}67^+$- (in all the samples) and DCX^+- (only in the *APP/PS1* and $App^{NL\text{-}G\text{-}F}$ dentate gyrus) cells were manually counted per section and average values per sample were calculated by averaging the values of all sections of the same sample. In Nestin:GFP- and DCX- (only in the Nestin:GFP dentate gyrus) immunostained samples, due to the strong signal, the mean intensity values instead of the cell counts were used. Similarly to before, 9-12 sections (with 40 µm distance between each two sections) per sample were used for quantification. Average values per sample were calculated by averaging the values of all sections of the same sample and the values of the control-injected sedentary animals were used for the normalization of all the samples.

For image acquisition of the cleared brain sections, a CSU-X1 spinning disk confocal microscope (tile-scan/z-stack, 10x plan fluor NA 0.3, 488nm laser line) (Nikon, Belgium) was used and 3D rendering of z-stacks was carried using Imaris x64 software (Bitplane, Switzerland). Briefly, GFP^+-cells were automatically identified as 10 µm 'spots' based on size and intensity thresholds were evenly applied for all samples. Reconstructed surfaces were volume-filtered to exclude those not belonging to the dentate gyrus. Spots up to 10 µm close to the dentate gyrus surface were considered for quantification. Values were normalized against the average of the scramble-injected group.

Video files were prepared in Imaris at a 360° angle and at 200 frames of horizontal movement, and saved at 24.000 frames per second and at 640 x 480 VGA.

For quantification of colocalized pre/post-synaptic puncta, images acquired with a 40x oil lens were subjected to deconvolution and maximum intensity projections of z-series were created with the Imaris x64 software. Dots were filtered by size (0.1-0.93μm^3) and the number of contact sites and the size of the analyzed area were calculated per image.

For assessing dendritic arborization, images of $mCHERRY^+$- and GFP^+- cells were acquired by regular confocal microscopy in vibratome-prepared sections. Branching points were counted manually, while the FIJI software was used for quantification of total dendritic length in the same cell. For assessing spine density, dendritic images of mCHERRY-labeled cells were acquired using the Zeiss LSM880 Airyscan super-resolution system (Carl Zeiss, Belgium), while dendritic images of GFP-labeled cells were obtained with a Leica TCS SP8 X microscope (Leica Microsystems, The Netherlands). More specifically, images of labeled dendritic processes at the outer molecular layer were acquired at 0.2 µm intervals with a 63x oil lens and a digital zoom of 2 (Zeiss LSM880 Airyscan) or at 0.1 µm intervals with a 40x oil lens and a digital zoom of 6 (Leica TCS SP8 X). Images were subjected to deconvolution and maximum intensity projections of z-series were created with the Imaris x64 software. The length of each dendritic segment was determined by tracing the center of the dendritic shaft and the number of spines was counted automatically from the two-dimensional projections. The linear spine density was calculated by dividing the total number of spines by the length of the dendritic segment.

RenCell cultures and transfections

RenCell VM human NPCs (Millipore, MA, USA) were cultured according to the manufacturer's instructions. Differentiation was induced by withdrawing growth factors (FGF-2 and EGF) from culture media. For cell transfections, 40-60% confluent cultures were transfected with miR-132 mimic and control oligonucleotides (at 0.1 pmol or 0.01pmol, depending on the experimental conditions, Dharmacon, Horizon Discovery, UK) or miR-132 antisense inhibitor and control oligonucleotides (at 50 pmol, Dharmacon, Horizon Discovery, UK) using lipofectamine RNAiMAX (ThermoFisher Scientific, Belgium) according to the manufacturer's instructions. Cells were collected for RNA extraction or fixed for immunostaining three days post transfection. For miR-132 inhibition experiments, differentiation was induced 24 h post transfection.

Neural induction of human embryonic pluripotent stem cells

Routine culturing and maintenance of human embryonic stem cells (EPSCs) (H9-GFP) (Espuny-Camacho et al., 2013, 2017) was performed using E8-flex growth medium (ThermoFisher Scientific, Belgium). Cells were maintained in a humidified chamber at 37^{o}C with 5% CO_2 and passaged every 4-5 days with 0.5 mM EDTA. Neural induction of human pluripotent stem cells (NPCs) was carried out according to a previously published protocol (Shi et al., 2012) with some modifications. Briefly, on DIV (days *in vitro*) -2 of neural induction, cells were enzymatically dissociated with StemPro Accutase cell dissociation reagent (Biolegend, CA, USA) and single cells were plated (1.5 x 10^6/well) in Matrigel-coated (Corning, Sigma-Aldrich, Belgium) 6-well plates in mTeSR1 growth medium (STEMCELL Technologies, France) supplemented with 10 mM Y-27632 ROCK inhibitor (Calbiochem, CA, USA). On DIV0, for initiation of neural induction, the culture medium was replaced with neural maintenance medium supplemented with 1 µM StemMACS LDN-193189 (Miltenyi, Biotec, Netherlands) and 10 µM SB431542 (STEMCELL Technologies, France). Neural induction was carried out for 12 days with daily replacement of growth media. After the neural induction, neuroepithelium was passaged three times

using Dispase-II (Roche, Belgium) to enrich for neural rosettes. Culture medium was supplemented with 20 ng/ml FGF (PeproTech, Belgium) during the first Dispase-II step for expansion. Around DIV29, neural rosettes were dissociated using the StemPro Accutase cell dissociation reagent and plated on laminin-coated culture dishes in neural maintenance medium for further maturation. RNA samples were collected on day DIV-2 (PSCs), day DIV29 (NPCs) and DIV60 (neurons).

Preparation of $A\beta_{1-42}$ oligomers and neuronal precursor cell treatment

Oligomerization and characterization of $A\beta_{1-42}$ was carried out as previously described (Brkic et al., 2015; Kuperstein et al., 2010). Briefly, $A\beta_{1–42}$ (A-1163-1, rPeptide, GA, USA) or scrambled $A\beta_{1–42}$ (A-1004-1, rPeptide, GA, USA) were dissolved at a concentration of 1 mg ml^{-1} in hexafluoroisopropanol (HFIP, Sigma-Aldrich, Belgium). A gentle stream of nitrogen gas was used to evaporate HFIP. The resulting pellet was resuspended in DMSO, and buffer was exchanged with Tris-EDTA using a 5 ml HiTrap desalting column (GE Healthcare, Belgium) according to the manufacturer's instructions. Determination of the eluted peptide concentration was performed using the Bradford method (Bio-Rad, Belgium). The eluted peptide was allowed to aggregate for 2 h at room temperature. EPSC-derived human neuronal precursor cells were incubated in neural maintenance medium containing 5 µM $A\beta_{1-42}$ or scramble control peptide for 72 h. Six biological replicates per treatment were used.

Treatment of human neuronal precursor cells with AD and control serum

Serum incubation of human neuronal precursors was performed as previously described (Maruszak et al, 2017, BioRxiv 10.1101/175604). More specifically, the multipotent human hippocampal progenitor/stem cell line HPC0A07/03C (ReNeuron, UK), derived from the first trimester female fetal hippocampal tissue following medical termination and in accordance with UK and USA ethical and legal guidelines, was obtained from Advanced Bioscience Resources (Alameda, CA, USA) and conditionally immortalized by introducing the c-myc-ERTAM transgene, which enables cells to proliferate indefinitely in the presence of epidermal growth factor (EGF), basic fibroblast growth factor (bFGF) and

4-hydroxy-tamoxifen (4-OHT). Removal of these factors induces spontaneous differentiation into neurons, astrocytes or oligodendrocytes. 24 h after seeding, proliferation medium containing EGF, bFGF and 4-OHT was replaced with proliferation medium additionally supplemented with 1% serum. Serum information can be found in Table S4. After 48 h of proliferation, differentiation was induced by replacing culture medium with medium supplemented with 1% serum but devoid of EGF, bFGF and 4-OHT. Each serum treatment was performed in triplicates. Samples were collected for RNA isolation after 7 days of differentiation.

RNA isolation, reverse transcription and real-time PCR

The dentate gyrus from adult mouse brain was microdissected as previously described (Hagihara et al., 2009). RNA extraction from whole dentate gyri was performed using the miRVana Paris Kit (Life Technologies, Belgium) according to the manufacturer's instructions. Briefly, tissue was homogenized in 350 µl cell disruption buffer supplemented with protease and phosphatase inhibitors. Following denaturation, addition of acid phenol:chloroform, incubation, and centrifugation, 1.25 volumes of ethanol 100% were added to the aqueous phase. The samples were then loaded on miRVana spin columns and processed according to the manufacturer's instructions. For isolating RNA from cultured cells, cells were first collected in 1 ml Trizol (Thermo Fisher Scientific, Belgium). Following incubation in chloroform and centrifugation 1.25 volumes of ethanol 100% were added to the aqueous phase and the samples were loaded and processed on miRVana spin columns like before. FACsorted cells were initially collected in RNAprotect Cell reagent (Qiagen, Netherlands) and following brief centrifugation, cell pellets were processed using the miRNeasy Micro kit (Qiagen, Netherlands) according to the manufacturer's instructions. Reverse transcription of 200 ng (mRNA) or 100 ng (miRNA) RNA was performed using the Superscript II reverse transcriptase (ThermoFisher Scientific, Belgium) for protein-coding transcripts and the Universal cDNA synthesis kit (Exiqon, Qiagen, Denmark) for miRNAs. Real-time semi-quantitative PCR was performed using the SensiFast Sybr No-Rox kit (Bioline, UK) for coding transcripts and the Sybr Green mastermix and LNA PCR primers (Exiqon, Qiagen, Denmark) for miRNAs.

Mean expression of two housekeeping genes was used for all normalizations (U6 snRNA, RNU5G for miRNAs, *Actb* and *Gapdh* for murine mRNAs, and *18S* and *GAPDH* for human mRNAs). The primer sequences can be found in Table S3. Cp (crossing points) were determined by using the second derivative method. Fold changes were calculated with the ΔΔCt method (Livak and Schmittgen, 2001).

Adult dentate gyrus dissociation for Fluorescence Activated Cell Sorting (FACS) of Nestin:GFP$^+$ cells

Dentate gyri (each sample consisted of 1 full dentate gyrus; right and left hemisphere) were first dissected and minced in Hibernate A Low Fluorescence (BrainBits, IL, USA) on ice. Tissue dissection was carried out in 20U/ml papain and 50U/ml DNaseI (Worthington, NJ, USA) for 20 min at 37^{o}C. The enzymatic digestion was stopped by incubating the samples in 10 mg/ml ovomucoid solution (Worthington, NJ, USA), cells were dissociated by trituration, filtered through a 70 µm nylon mesh, span down and eventually resuspended in ice-cold Hibernate A. Debris and myelin removal was performed using the adult brain dissociation kit (Miltenyi Biotec, Netherlands) according to the manufacturer's instructions. Finally, cells were resuspended in ice-cold Hibernate A and dead cells were stained with propidium iodide (ThermoFisher Scientific, Belgium). GFP$^+$- and GFP$^-$-cells were sorted in a FACS Aria III (BD Biosciences, CA, USA) in RNase-free eppendorfs (in bulk) or in 96-well plates (in single) for downstream analysis.

Behavioral testing

For contextual fear conditioning assessment, a passive avoidance protocol was employed using a two (an illuminated and a dark one, separated by a guillotine door)-compartment box with a shock grid (Callaerts-Vegh et al., 2015; D'Hooge, 2005). Briefly, dark-adapted, single-housed 9-month old male mice were placed in the illuminated box and latency to enter the dark compartment was recorded. Upon entry into the dark compartment (all four paws inside), the door was closed and a 2 s foot shock (0.2 mA) was applied. The mice were then immediately removed from the box and placed back in their home cage. Twenty four hours later, the dark-adapted mice were again placed in the illuminated box

and latency to enter the dark compartment was measured as retention of contextual memory. A maximum of 300 s was noted in case the animal would not enter within the first five minutes.

Pattern separation in 9-month old male mice was measured using an adapted fear conditioning protocol (van Boxelaere et al., 2017; Nakashiba et al., 2012). Briefly, animals were fear conditioned in a specific context (A) by placing them in a conditioning cage (25 x 25 x 25 cm) fitted with stainless steel grid floors to deliver mild foot shocks and located in sound-attenuating cubicles (Panlab Startle & Fear Combined System (Panlab, Spain)). Animal movement was monitored by a motion-sensitive floor (the degree of motion could range from 0 to 100) connected to an interfaced computer using Panlab Freezing v1.2.0 software. Freezing was counted if registered movement remained below the arbitrarily defined threshold of 2.5 for at least 1 s. Before testing, animals were placed in a holding area for 30 min for habituation. Contextual fear conditioning consisted of 3 days conditioning in context A, followed by 2 days context testing (A, B, and C, see Figure 7B). In contextual fear acquisition (Days 1-3), mice were placed in context A and after 3 min exploration, a foot shock (2 s; 0.5 mA) was delivered. One minute later, mice were removed from the testing box and placed in their housing cage. Freezing was measured during the 3 min interval preceding the shock.

To determine the specificity of contextual fear conditioning, freezing behavior in contexts A, B and C was recorded during the generalization testing (Days 4–5). On day 4, mice were placed in context A without shocks for 3 min, then removed and placed in a housing cage. 120–150 min later, mice were placed in context B (same features as A, except for an inserted A-frame roof made of black cardboard) and, eventually following the same procedure as before, in context C (change in tactile, olfactory and visual dimension). The testing order between the four groups was randomized to minimize testing time effect, but all animals were tested first in one context before the next context was presented. On day 5, the same procedure was followed but the order of context presentation was changed to B → A →C. Freezing was measured during a 3 min interval and freezing behavior in a similar (B) or a different (C) context was recorded as a measure of discrimination learning (pattern separation).

Temozolomide (TMZ) treatment

TMZ (Sigma-Aldrich, Belgium) solution (in 10% DMSO) was diluted in 0.9% NaCl to a concentration of 2.5 mg/ml. Control vehicle solution was similarly prepared using 10% DMSO in 0.9% NaCl without TMZ. TMZ or control vehicle were administered i.p. at a dose of 12.5 mg/kg of body weight once a day for 3 consecutive days, followed by 4 days of no injections (one cycle). ICV injections of miR-132 or control mimic were every time performed 2 days after the last TMZ or control vehicle injection of each cycle. After 4 cycles, mice were subjected to the avoidance test.

Smart-seq2 processing and single-cell library preparation

For FACS isolation of single cells, four miR-132-injected and four control-injected Nestin:GFP male mice were used and 94 cells were initially sorted per mouse. FACS-sorted cells were processed using the Smart-seq2 protocol (Picelli et al., 2013). Briefly, RNA was reverse-transcribed using biotinylated oligo-dT primers (IDT DNA, Belgium) and biotinylated template-switching (TSO) oligonucleotides (Exiqon, Qiagen, Denmark) and subsequently cDNA was preamplified using the KAPA HiFi Hot Start DNA Polymerase (KAPA Biosystems, Roche Diagnostics, Belgium) and biotinylated ISPCR primers (IDT DNA, Belgium). cDNA was purified using AMPURE XP Agencourt beads (Beckman Coulter, France), concentration was calculated with the Quantifluor dsDNA kit (Promega, Netherlands) and adjusted on an Echo 525 Liquid Handler (Labcyte, CA, USA). 100 pg cDNA per cell were used for library preparation with Nextera XT DNA Library Preparation Kit (Illumina, CA, USA). Finally, following purification on magnetic beads the libraries were multiplexed and sequenced using the Illumina NextSeq500 platform (Illumina, CA, USA).

Data processing

To confirm quality of the raw reads, a FastQC analysis (Version 0.11.5, https://www.bioinformatics.babraham.ac.uk/projects/fastqc/) was performed. Reads were aligned to the mouse mm10 genome (Ensembl Version 88) using STAR (Version 2.5.2 (Dobin et al., 2013)) with

default options. A count table was generated from the alignments using Subread/FeatureCounts 1.5.1 (Liao et al., 2014).

The count matrix was analyzed with Seurat 2.3.1 (Butler et al., 2018), using the following workflow: Cells with less than 200 genes or more than 6,000 genes (likely doublets) were removed, as well as cells whose mitochondrial gene expression accounted for more than 20% of the total gene expression of that cell. Genes found in less than 0.5% of cells were also excluded. Following this filtering, 709 of the original 752 cells remained (with a median read depth of 630,131 reads per cell and median of 2,646 genes per cell). Data was log-normalized and scaled by a factor of 10,000. The normalized count data was subsequently regressed on the number of reads. Principal component analysis (PCA) was performed using the top 1,438 highly variable genes. The first 30 PCAs were used to identify clusters (using default parameters). Data was visualized using t-Distributed Stochastic Neighbor Embedding (t-SNE). Cluster markers were determined by a differential expression analysis of each cluster versus all other clusters combined (Table S5; ClusterMarkers). Seurat's "AddModuleScore" function, with default parameters, was used to calculate gene set scores of cell type-specific markers extracted from previous studies (Table S5; LiteratureMarkers) (Artegiani et al., 2017; Hochgerner et al., 2018; Zeisel et al., 2018). Boxplots of these scores were used to assign each cluster to a cell type (for summary data see Table S5; ModuleScore). We confirmed these assignments by comparing our cluster markers to unique markers of cell type defined by the aforementioned studies to ensure that there was no ambiguity in the assignment of cell types. Gene differential expression between experimental (miR-132 overexpression) and control conditions (within each cell population) was performed (Table S6). Differential expression (for analysis of cluster markers and for analysis between controls and experimental conditions) was performed as follows: p-values were calculated using a Wilcoxon rank-sum test (using Seurat's "FindMarkers" function), and corrected for multiple testing using a Bonferroni correction. Log fold changes were calculated using the natural logarithm. Genes with adjusted p-values of < 0.05 were considered significantly differentially expressed. All sequencing data reported in this study will be deposited in the NCBI Gene Expression Omnibus upon publication.

Functional enrichment analysis was performed by using Ingenuity Pathway Analysis (IPA, Ingenuity Systems Inc., Redwood City, CA, USA). By convention, the 150 transcripts with the most negative ('Downregulated Transcripts', left side of x-axis) or most positive ('Upregulated Transcripts', right side of x-axis) log fold changes after differential gene expression (comparing miR-132-overexpression to control samples) were selected per cluster for analysis.

Figure 1

Click here to access/download;Figure;Figure 1.jpg

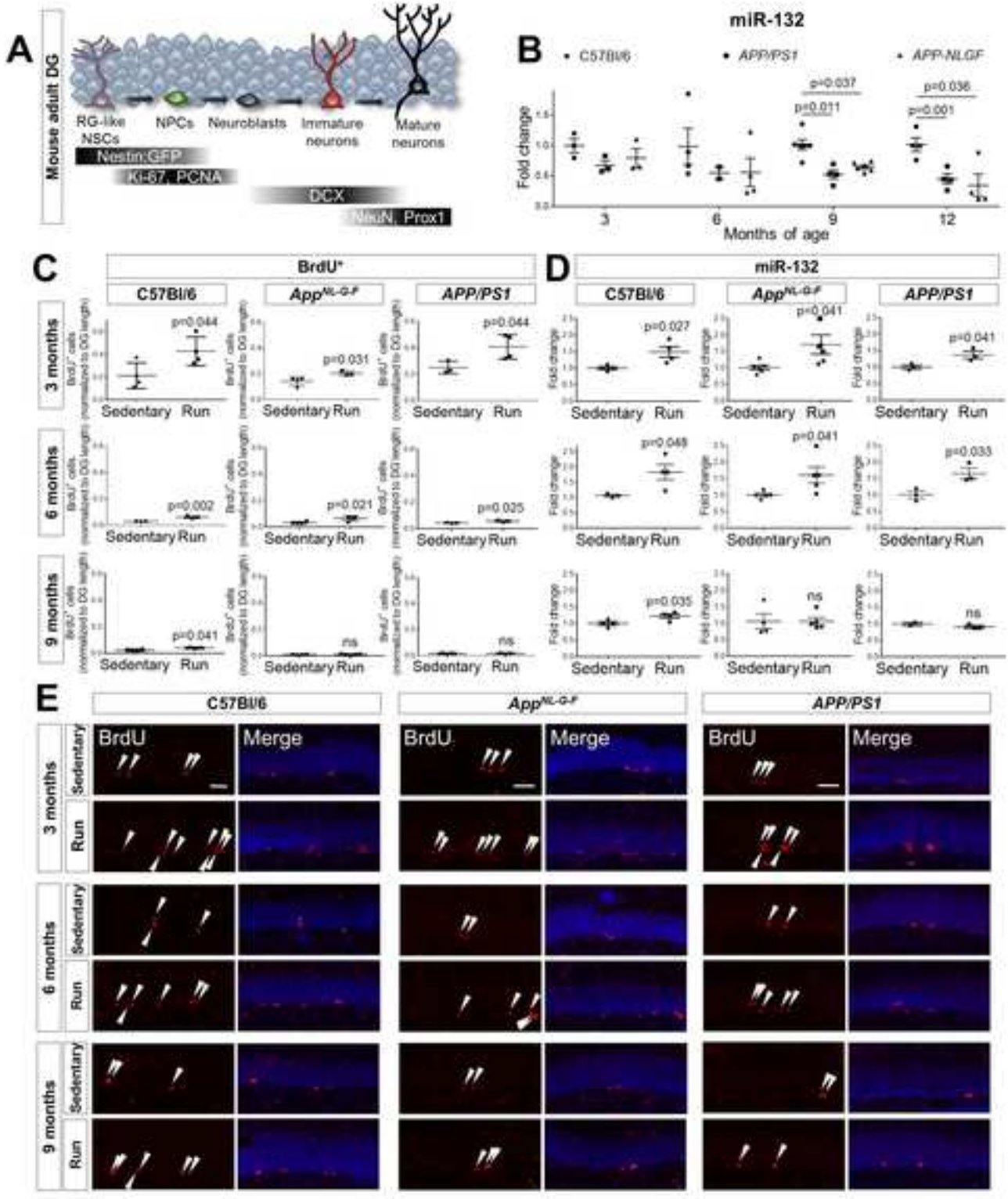

Figure 2

Click here to access/download;Figure;Figure 2.jpg

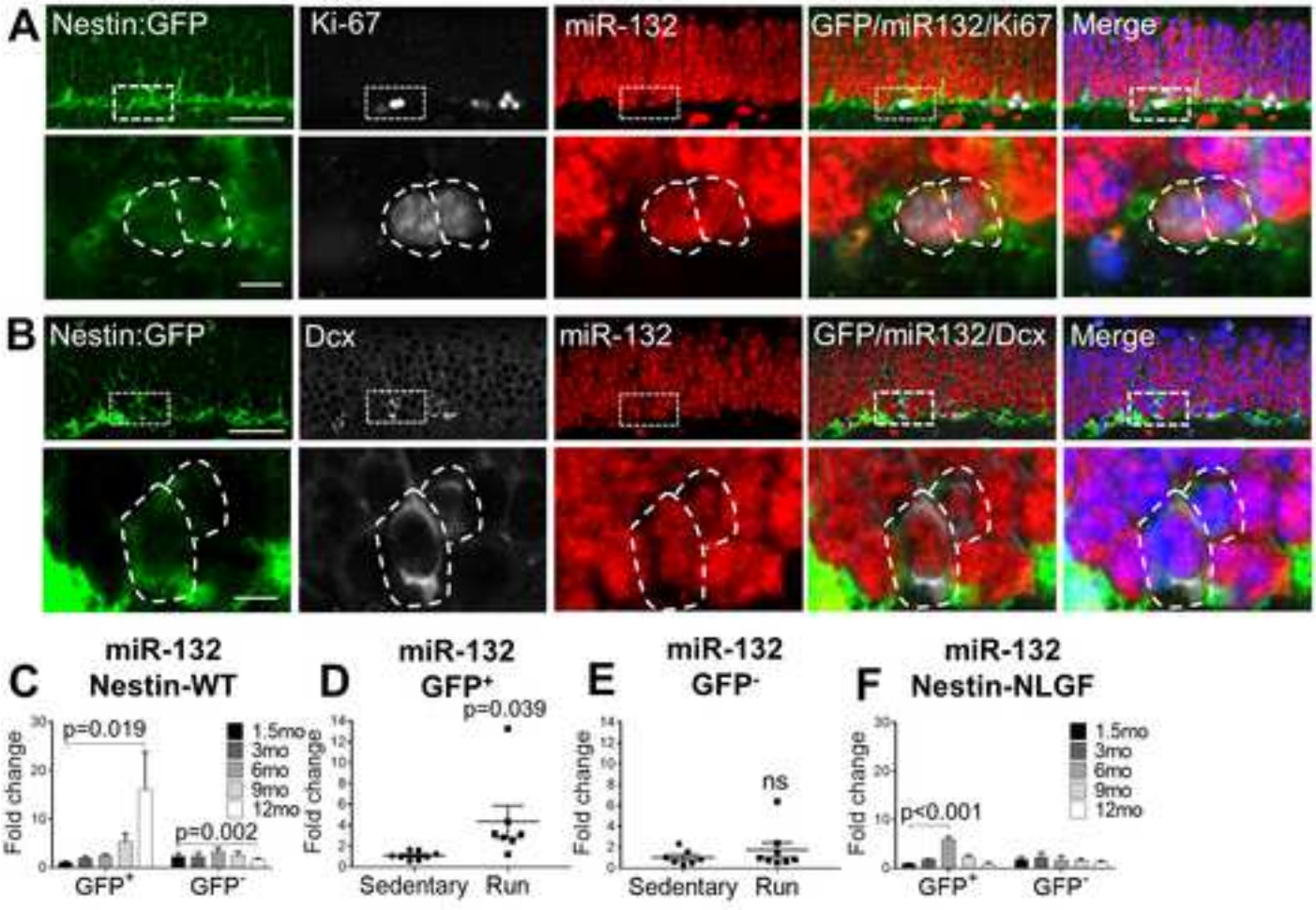

Figure 3

Click here to access/download;Figure;Figure 3.jpg

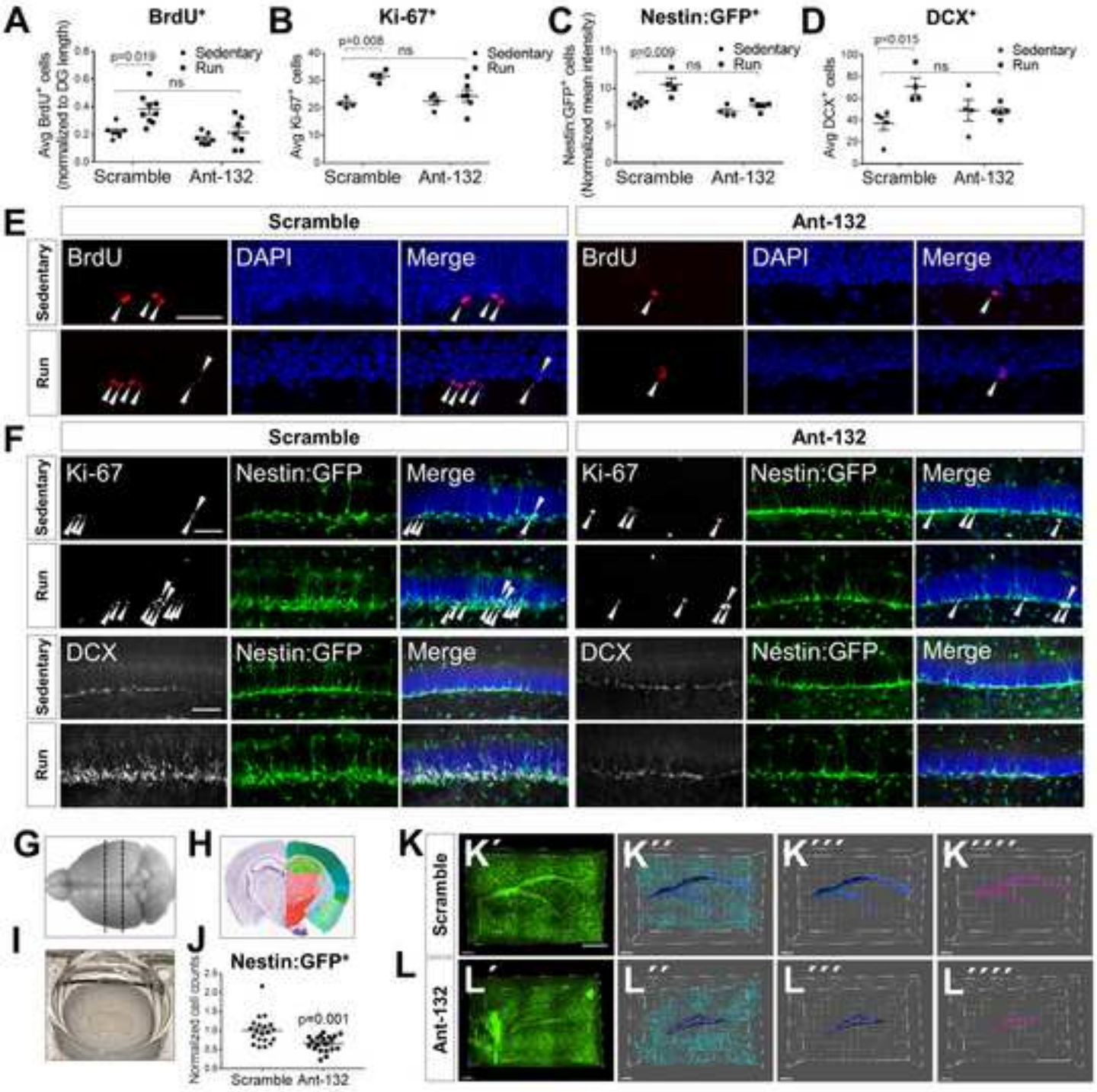

Figure 4

Click here to access/download;Figure;Figure 4.jpg

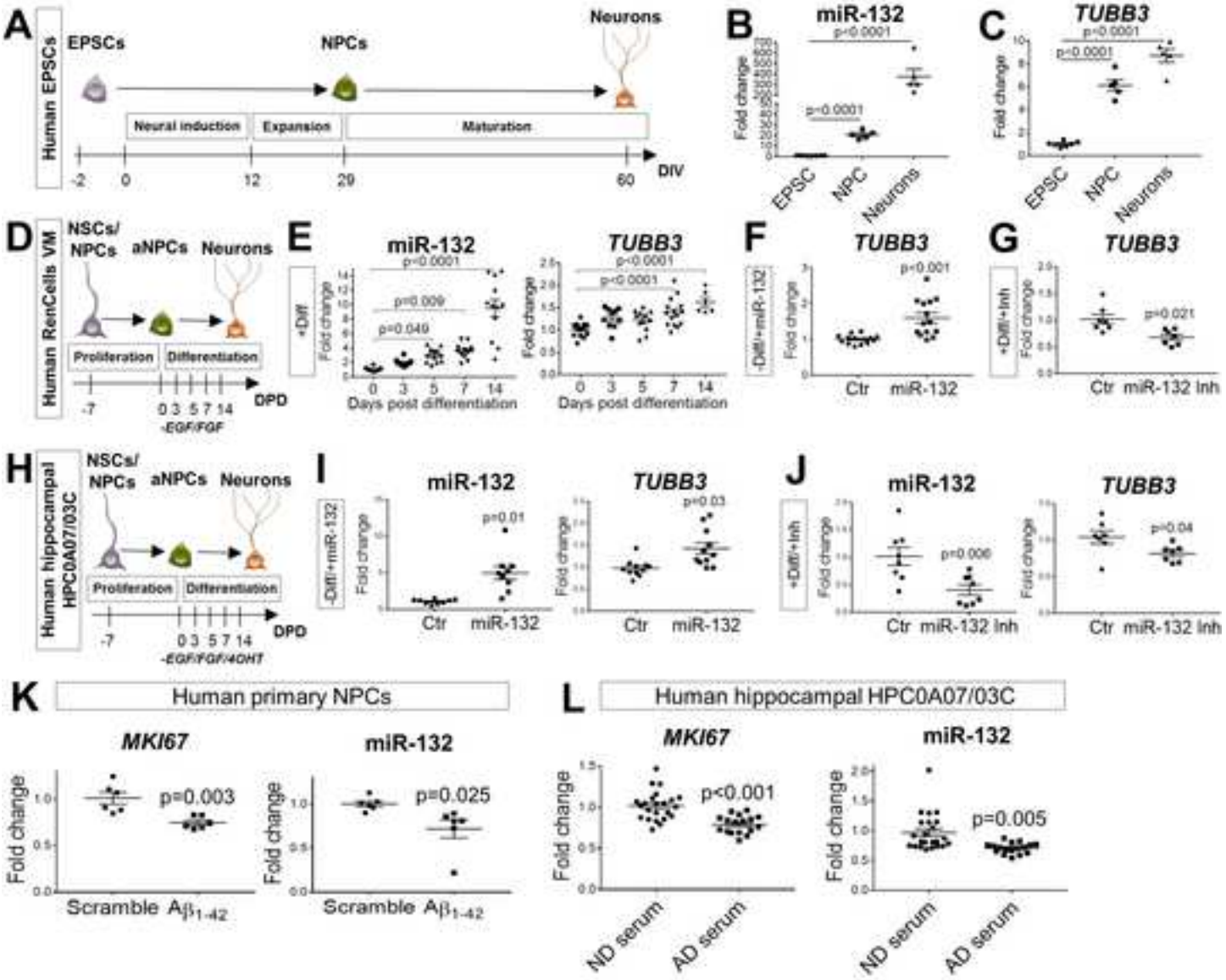

Figure 5

Click here to access/download;Figure;Figure 5.jpg

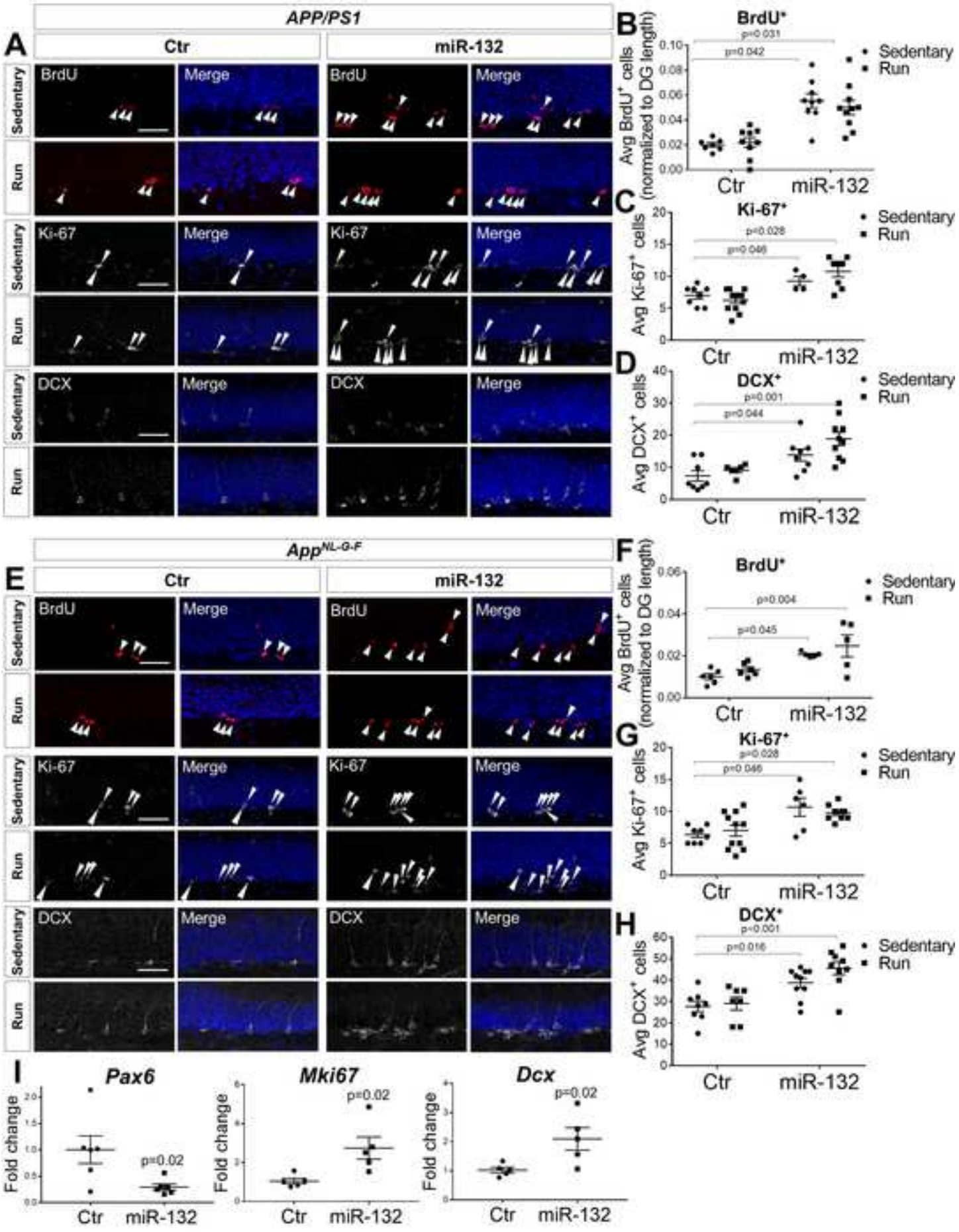

Figure 6

Click here to access/download;Figure;Figure 6.jpg

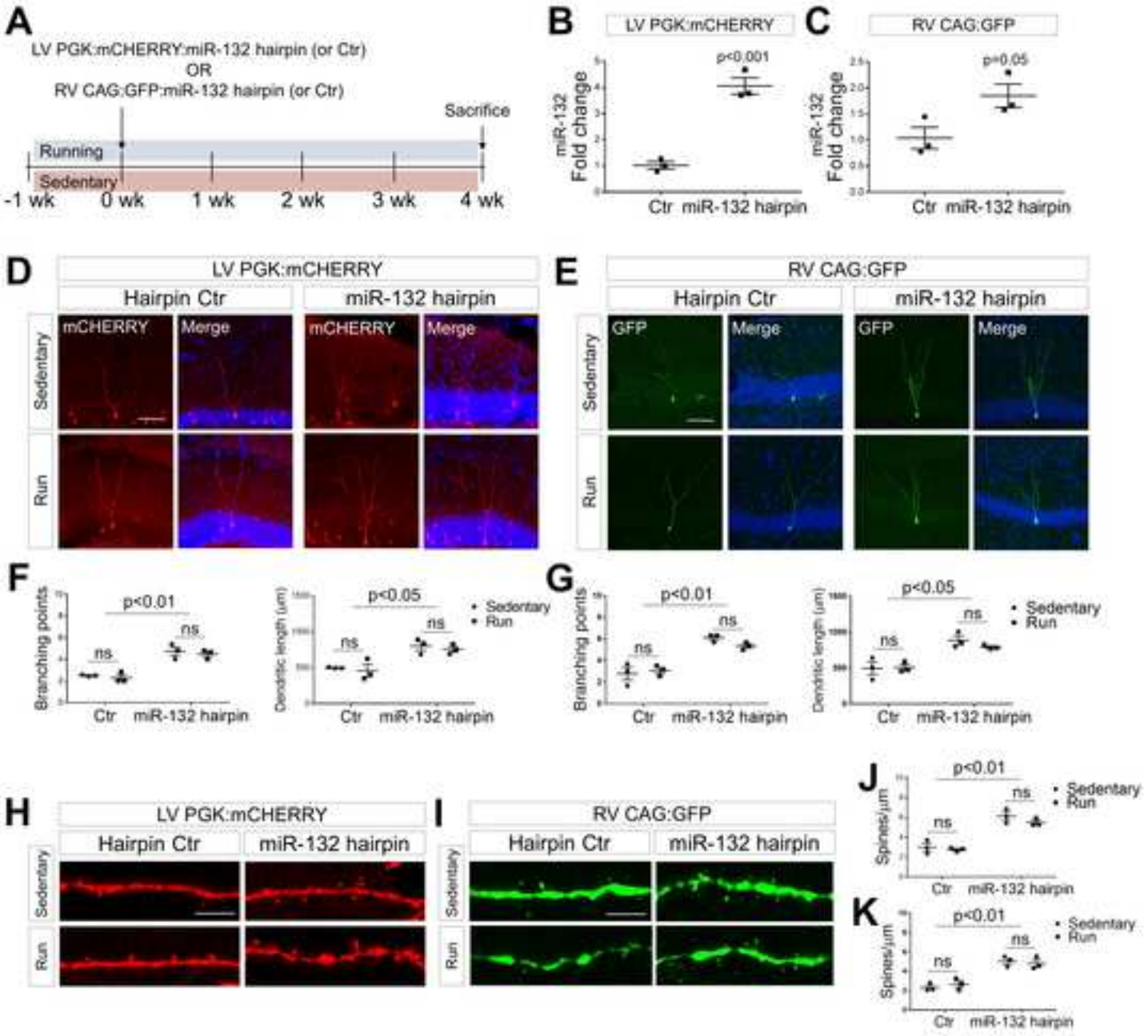

Figure 7

Click here to access/download;Figure;Figure 7.jpg

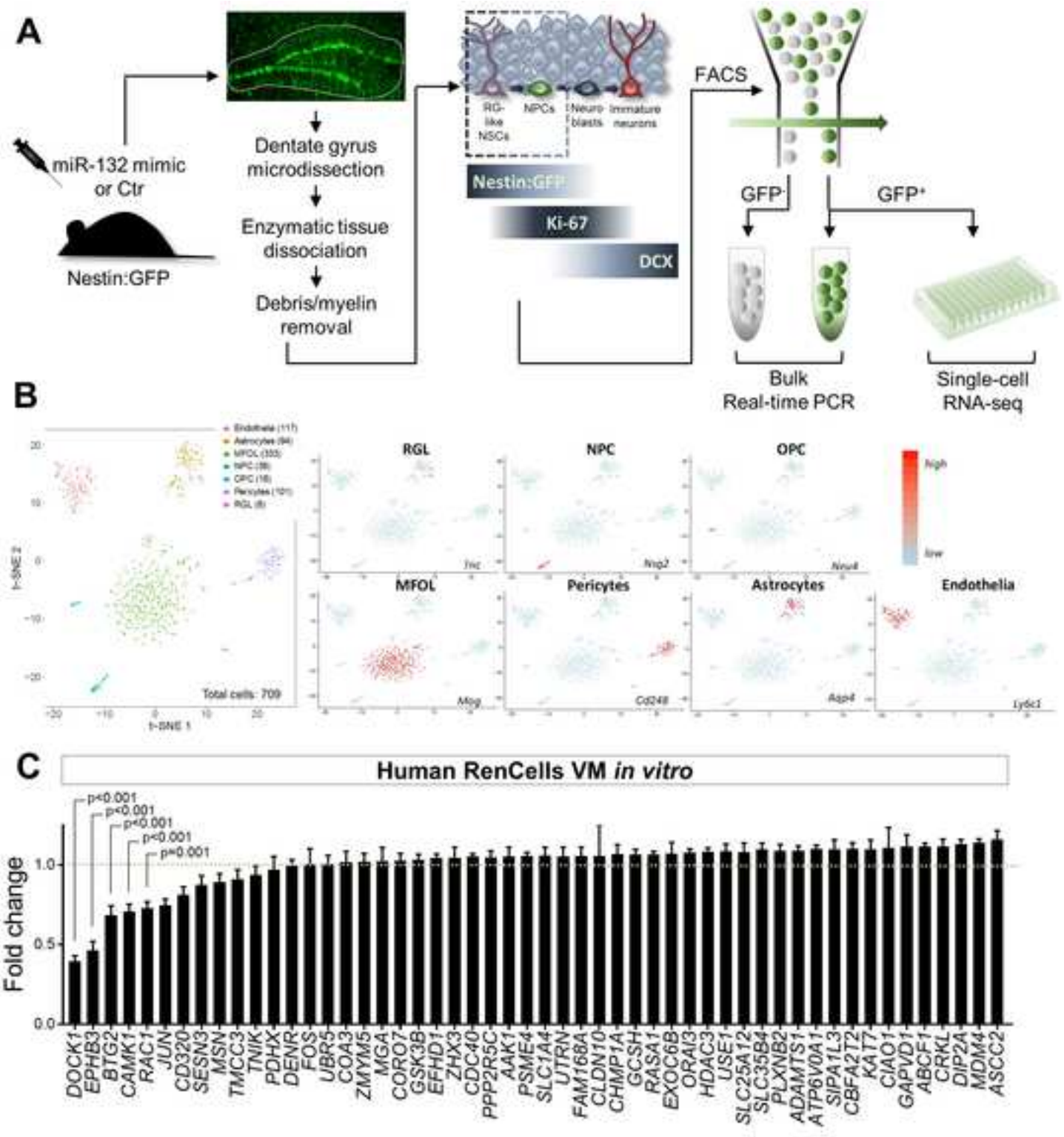

Figure 8

Click here to access/download;Figure;Figure 8.jpg

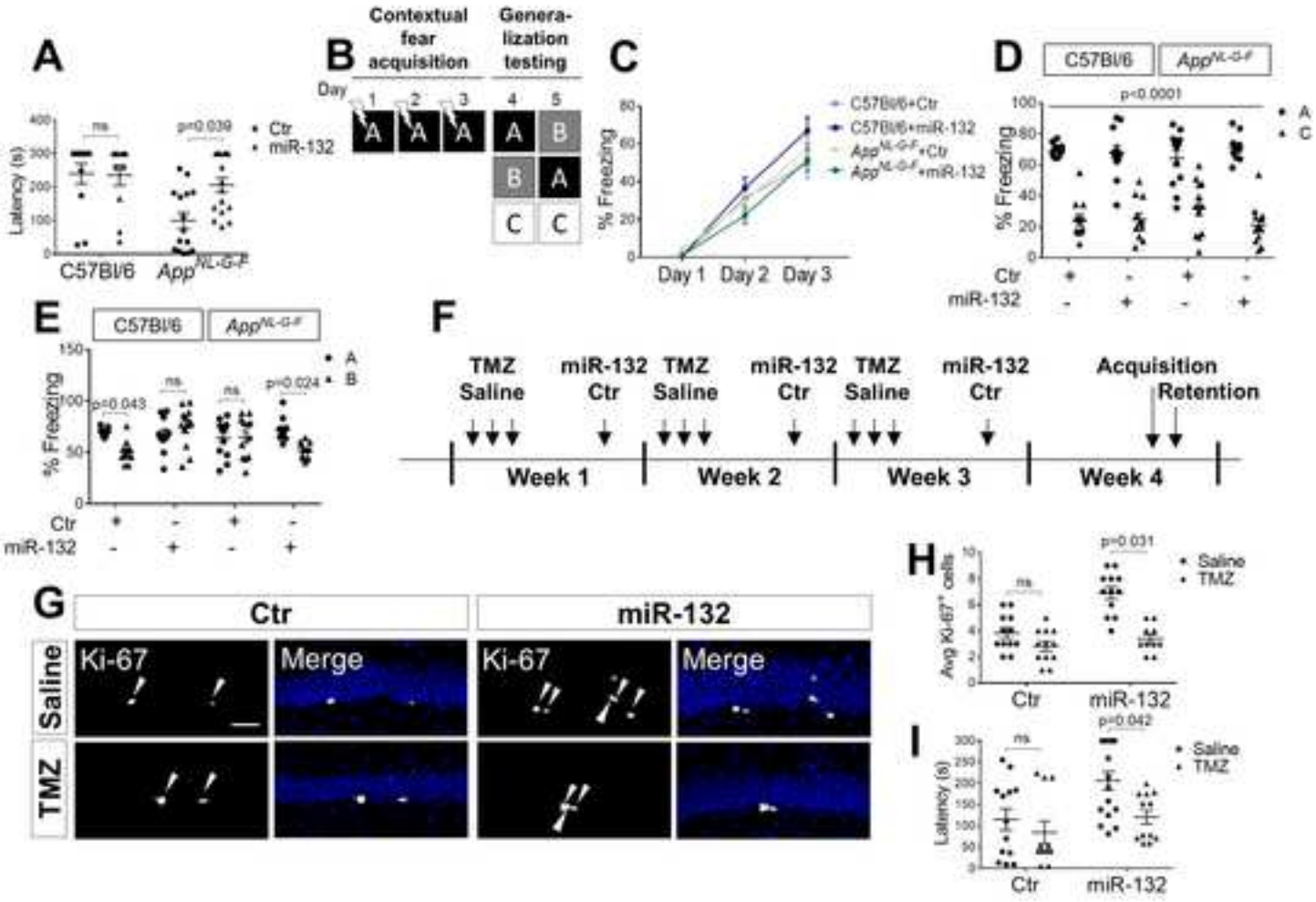

Supplemental Information

Supplementary Figures

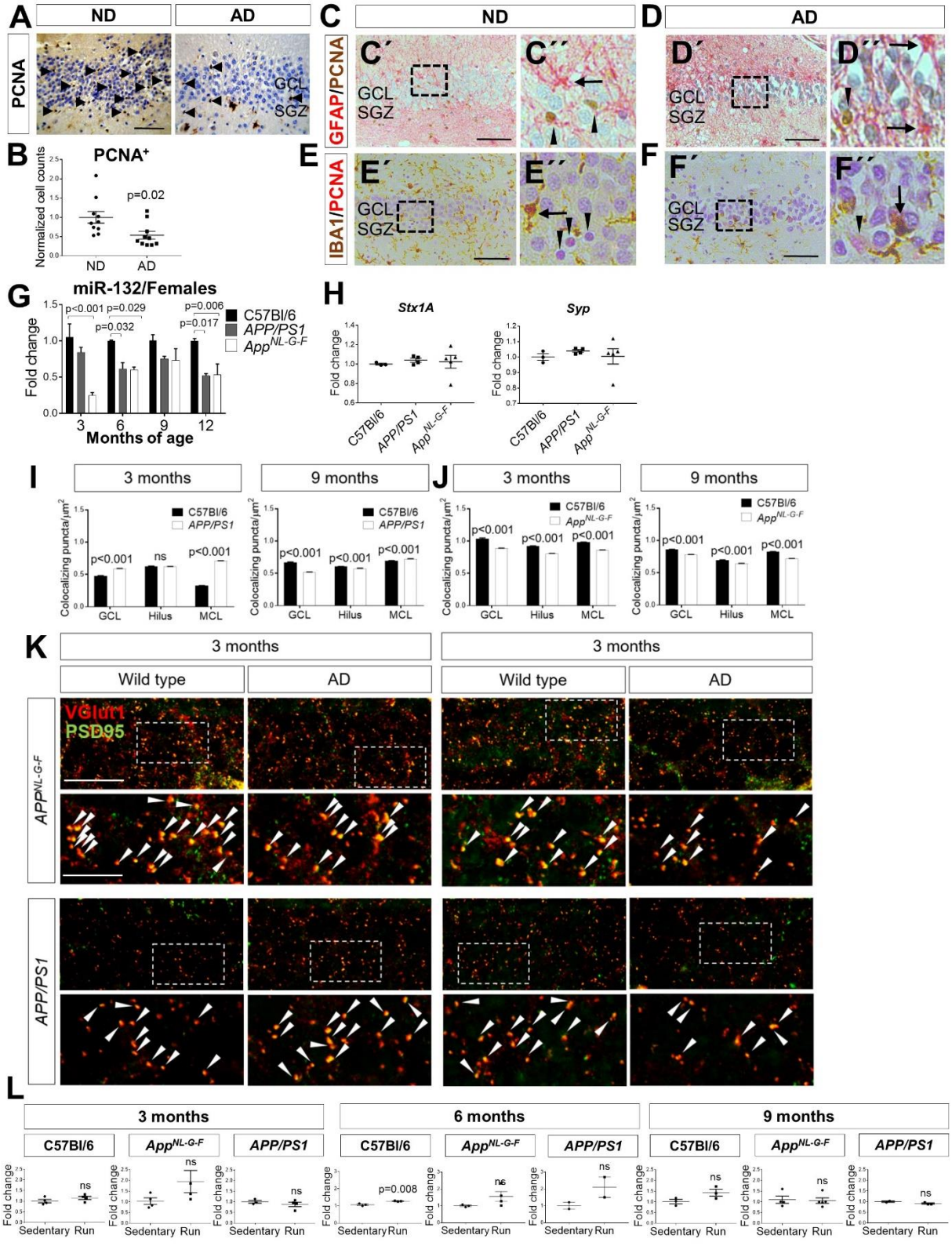

Figure S1. Related to Figure 1.

A. Immunohistochemical labeling using the PCNA cell proliferation marker in the dentate gyrus of non-demented (ND) control individuals and Alzheimer's (AD) patients. Arrowheads indicate $PCNA^+$-cells at the subgranular zone (SGZ) and the granular cell layer (GCL) as previously reported (Boldrini et al., 2018). Scale bar, 50 µm. B. Quantification of $PCNA^+$-cells counts. Values were normalized to 1000 total cell counts per sample (see STAR Methods). N=10 samples per group. C, D. GFAP/PCNA double immunolabeling in the dentate gyrus of non-demented (ND) control individuals (C) and Alzheimer's (AD) patients (D). C'' and D'' show magnified views indicated by dashed rectangles in C' and D', respectively. Arrows indicate $GFAP^+$-astrocytes, while arrowheads indicate $PCNA^+$-cells. SGZ, subgranular zone; GCL, granular cell layer. E, F. IBA1/PCNA double immunolabeling in the dentate gyrus of ND (E) and AD samples (F). E'' and F'' show magnified views indicated by dashed rectangles in E' and F', respectively. Arrows indicate $IBA1^+$-microglia and arrowheads indicate $PCNA^+$-cells. Scale bars, 50 µm. G. Semi-quantitative real-time PCR of miR-132 levels in the dentate gyrus of C57Bl/6, *APP/PS1* and $App^{NL\text{-}G\text{-}F}$ female mice at 3, 6, 9 and 12 months of age. N=3-6 mice per time point. H. Semi-quantitative real-time PCR of syntaxin 1A (*Stx1A*) and synaptophysin (*Syp*) in the dentate gyrus of 12-month-old C57Bl/6, *APP/PS1* and $App^{NL\text{-}G\text{-}F}$ mice. N=4-5 mice per group. I-K. Colocalization of $VGlut1^+$-presynaptic and $PSD95^+$-postsynaptic puncta in granular cell layer (GCL), hilus and molecular cell layer (MCL) of the dentate gyrus in C57Bl/6, APP/PS1 and $App^{NL\text{-}G\text{-}F}$ mice at 3 and 9 months of age. N=3 mice per time point. Arrowheads indicate double-positive puncta. Scale bars, 10 µm (lower magnification); 4 µm (higher magnification). L. Semi-quantitative real-time PCR of miR-212 levels in the dentate gyrus of C57Bl/6, *APP/PS1* and $App^{NL\text{-}G\text{-}F}$ sedentary control or running mice at 3, 6 and 9 months of age. N=3-6 mice per group. Values are presented as mean ± SEM. In (G, I, J), two-way ANOVA with Tukey's *post hoc* test for multiple testing were applied, in (H), one-way ANOVA with Tukey's multiple testing, and in (B, L), Student's t-test was used.

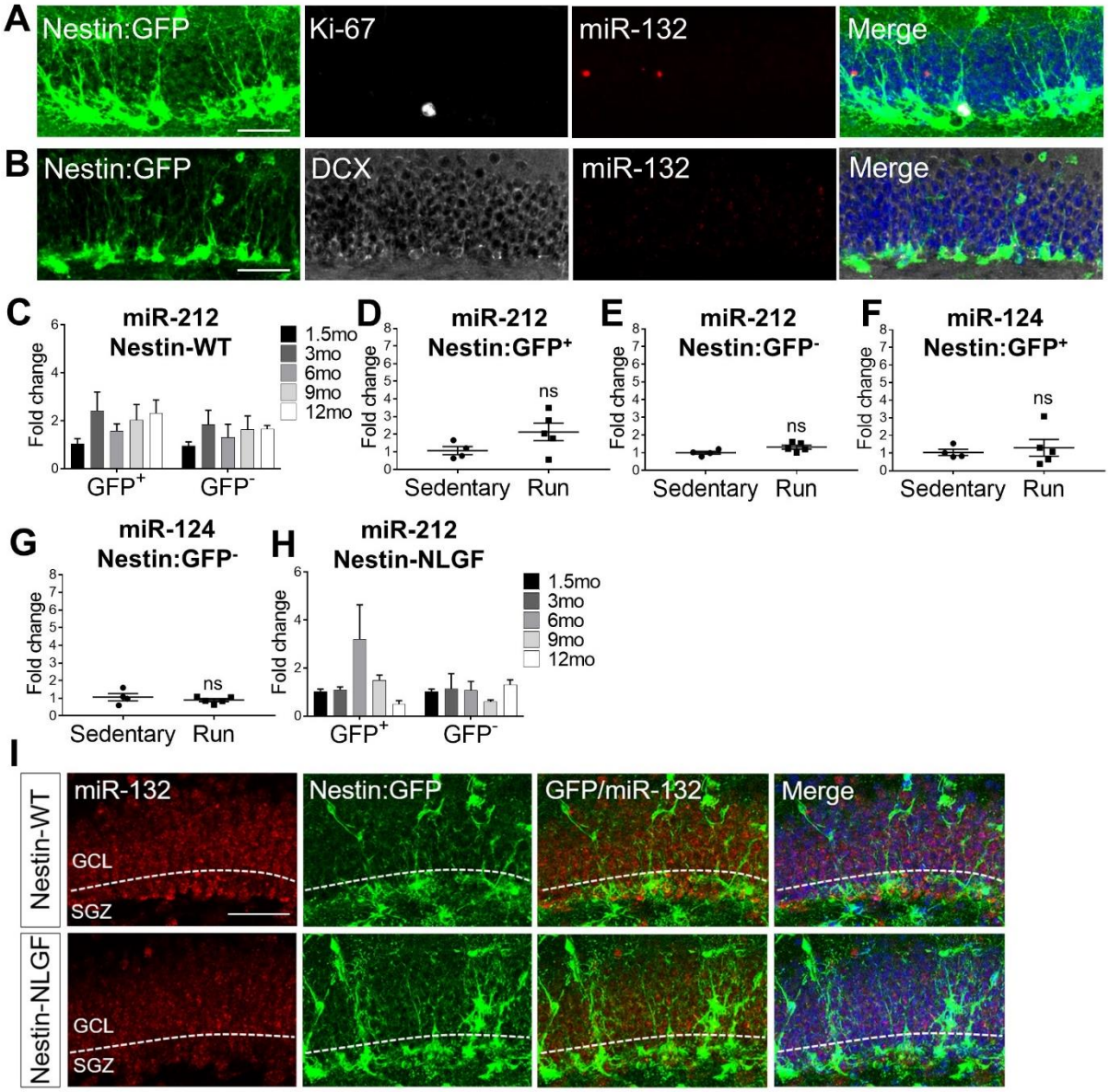

Figure S2. Related to Figure 2. A, B. *In situ* hybridization using a scramble control probe combined with Nestin and Ki-67 (A) or Nestin and doublecortin (DCX) (B) immunolabeling in the dentate gyrus of 3-month-old Nestin:GFP mice. Scale bar, 50 µm. C. Semi-quantitative real-time PCR of miR-212 levels in GFP^+ or GFP^-populations sorted from the dentate gyrus of Nestin:GFP mice at 1.5, 3, 6, 9 and 12 months of age. N=6-8 mice per time point. D, E. Semi-quantitative real-time PCR of miR-212 levels in GFP^+ (D) or GFP^- (E) populations sorted from the dentate gyrus of sedentary control or running Nestin:GFP mice at 3 months of age. N=5-6 mice per group. F, G. Semi-quantitative real-time PCR of miR-124 levels in

GFP$^+$ (F) or GFP$^-$ (G) populations sorted from the dentate gyrus of sedentary control or running Nestin:GFP mice at 3 months of age. N=5-6 mice per group. H. Semi-quantitative real-time PCR of miR-212 levels in GFP$^+$ or GFP$^-$populations sorted from the dentate gyrus of Nestin-NLGF mice at 1.5, 3, 6, 9 and 12 months of age. N=3-5 mice per time point. I. In situ hybridization for miR-132 in 9-month old Nestin:GFP wild-type (Nestin-WT) and AD (Nestin-NLGF) mice. GCL, granular cell layer; SGZ, subgranular zone. Scale bar, 50 µm. Values are presented as mean ± SEM. In (C, H), two-way ANOVA with Tukey's *post hoc* test for multiple testing were used, while in (D-G), Student's t-test was applied.

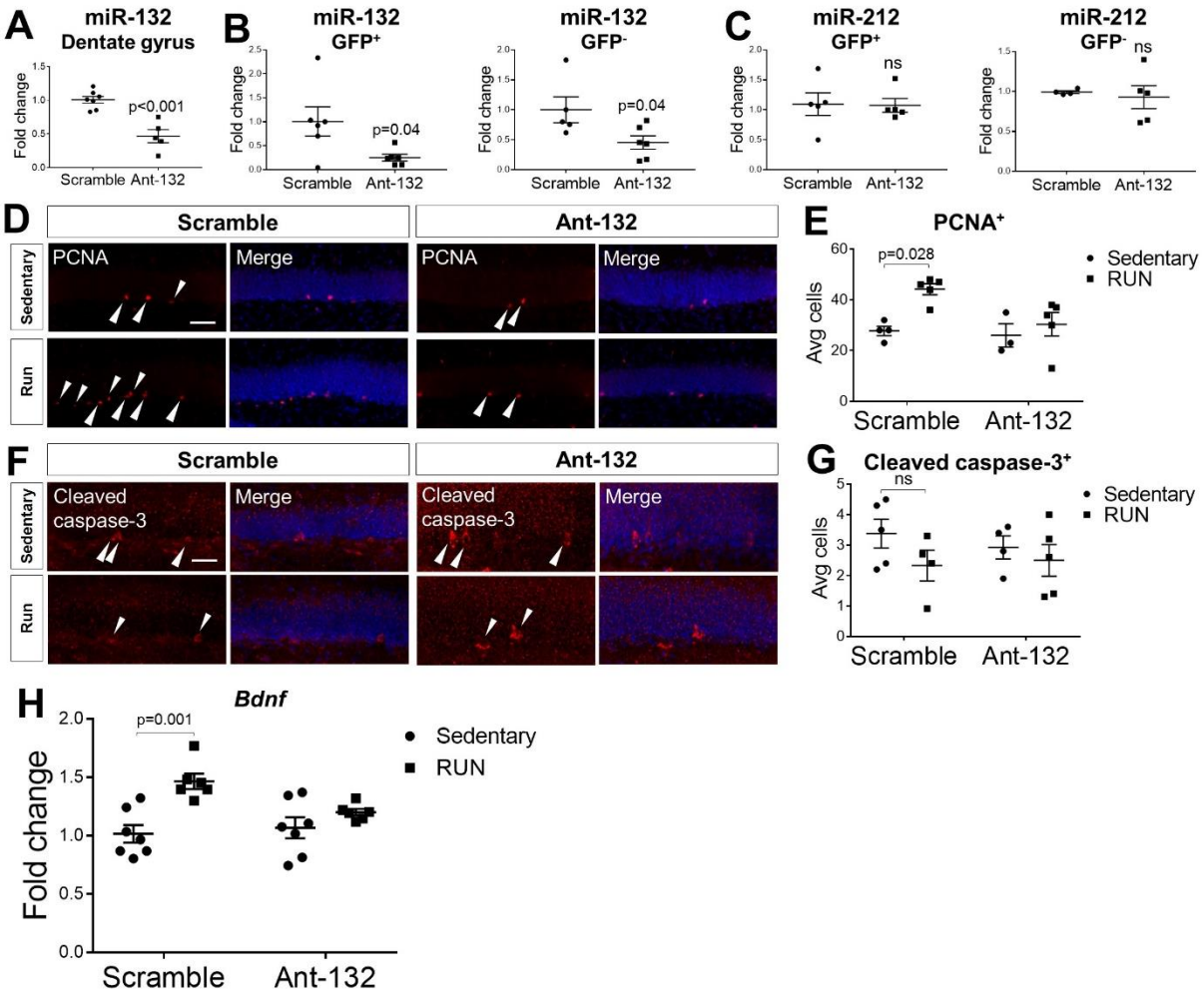

Figure S3. Related to Figure 3. A. Semi-quantitative real-time PCR of miR-132 levels in scramble- and Ant-132-injected 9-month-old C57Bl/6 mice prior to running. N=6 mice per group. B. Semi-quantitative real-time PCR of miR-132 levels in GFP$^+$- and GFP$^-$ -cells sorted from the dentate gyrus of Nestin:GFP

mice upon miR-132 knockdown prior to running. N=5 mice per group. C. Semi-quantitative real-time PCR of miR-212 levels in GFP^+- and GFP^- -cells sorted from the dentate gyrus of Nestin:GFP mice upon miR-132 knockdown prior to running. N=5 mice per group. D. $PCNA^+$-cells in the subgranular layer of the dentate gyrus of control- or Ant-132-injected, sedentary or running Nestin:GFP mice at 3 months of age. Scale bars, 50 µm. E. Quantification of $PCNA^+$-cells in (D). N=3-5 mice per group. F. Cleaved caspase-3^+-cells in the subgranular layer of the dentate gyrus of control- or Ant-132-injected, sedentary or running Nestin:GFP mice at 3 months of age. Scale bars, 50 µm. G. Quantification of cleaved caspase-3^+-cells in (F). N=3-5 mice per group. H. Semi-quantitative real-time PCR assessment of the levels of *Bdnf* in the dentate gyrus of control- or Ant-132-injected, sedentary or running Nestin:GFP mice at 3 months of age. N=5-7 mice per group. Values are presented as mean ± SEM. In (A-C), the Student's t-test was applied, while in (E, G, H), two-way ANOVA with Tukey's *post hoc* test for multiple testing were used.

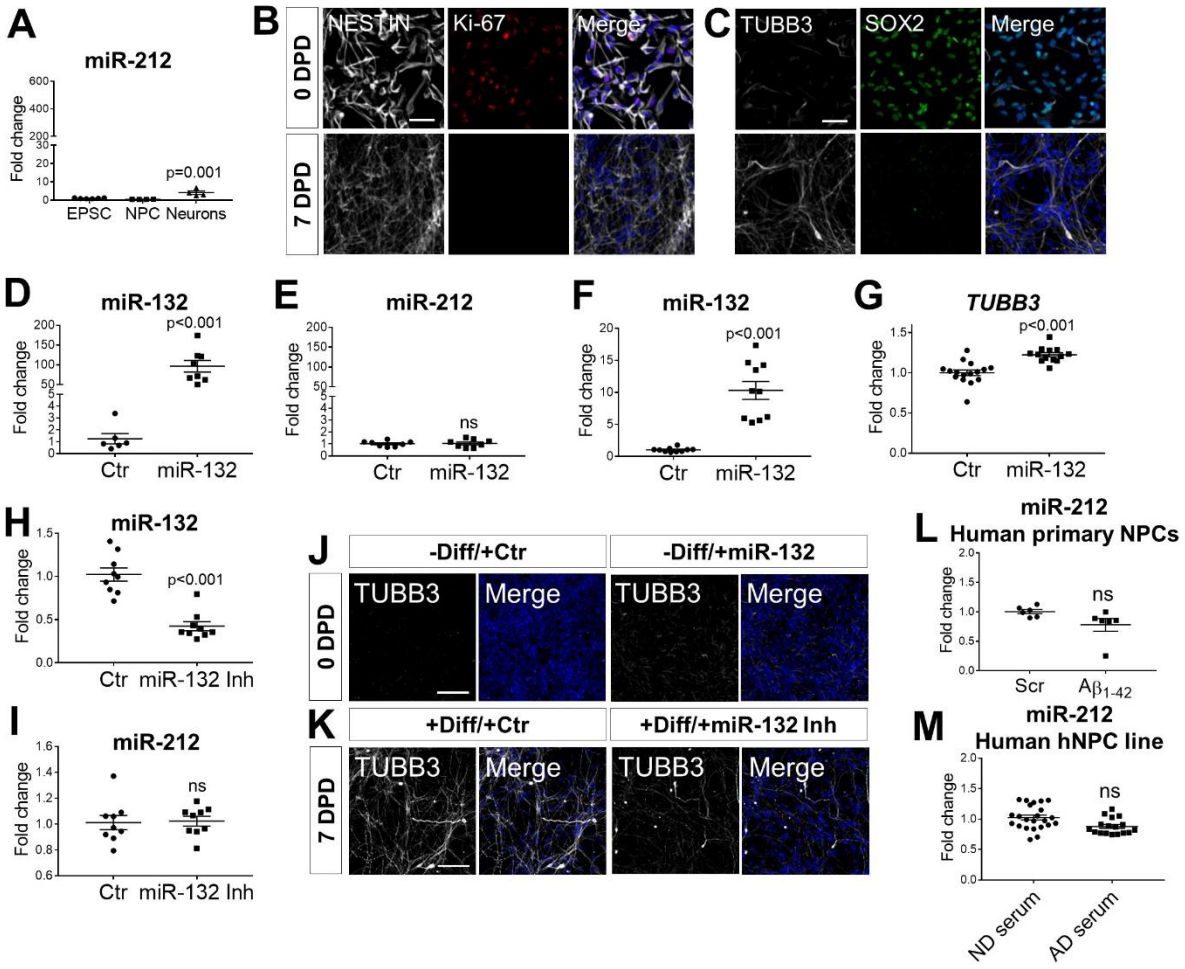

Figure S4. Related to Figure 4.

A. Semi-quantitative real-time PCR of miR-212 levels in human EPSCs, NPCs and mature neurons. N=3 independent experiments. B, C. Immunolabeling of NESTIN and Ki-67 (B) or TUBB3 and SOX2 (C) in human neuronal progenitors at 0 and 7 days post differentiation (DPD). Scale bars, 100 µm. D, E. Semi-quantitative real-time PCR of miR-132 (D) and miR-212 (E) levels upon transfection of undifferentiated human neuronal progenitors with 0.1pmol control (Ctr) or miR-132 mimic oligonucleotide (miR-132) 2 days post transfection. N=3 independent experiments. F. Semi-quantitative real-time PCR of miR-132 levels upon transfection of undifferentiated human neuronal progenitors with 0.01pmol control (Ctr) or miR-132 mimic oligonucleotide (miR-132) 2 days post transfection. N=3 independent experiments. G. Semi-quantitative real-time PCR of *TUBB3* levels upon transfection of undifferentiated human neuronal progenitors with 0.01pmol control (Ctr) or miR-132 mimic oligonucleotide (miR-132) 2 days post transfection. N=3 independent experiments. H, I. Semi-quantitative real-time PCR of miR-132 (H) and miR-212 (I) levels upon control or miR-132 inhibitor (miR-132 Inh) transfection of differentiating human neuronal progenitors 2 days post transfection. N=3 independent experiments. J, K. TUBB3 immunostaining in human neuronal progenitors transfected with miR-132 mimic without induction of differentiation (-Diff) (J) or inhibitor with differentiation induction (+Diff) (K) at 0 and 7 days post differentiation (DPD), respectively. Scale bars, 100 µm. L. Semi-quantitative real-time PCR of miR-212 in EPSC-derived human NPCs upon treatment with $A\beta_{1-42}$ oligomers and a scramble control peptide. N=6 biological replicates. M. Semi-quantitative real-time PCR of miR-212 in an established human hippocampal NPC (hNPC) line (HPC0A07/03CI) upon incubation with AD or control serum. N=23 (ND) and 17 (AD). Values are presented as mean ± SEM. In (A), one-way ANOVA with Tukey's *post hoc* test for multiple testing was employed, while in (D-I, L, M), the Student's t-test was applied.

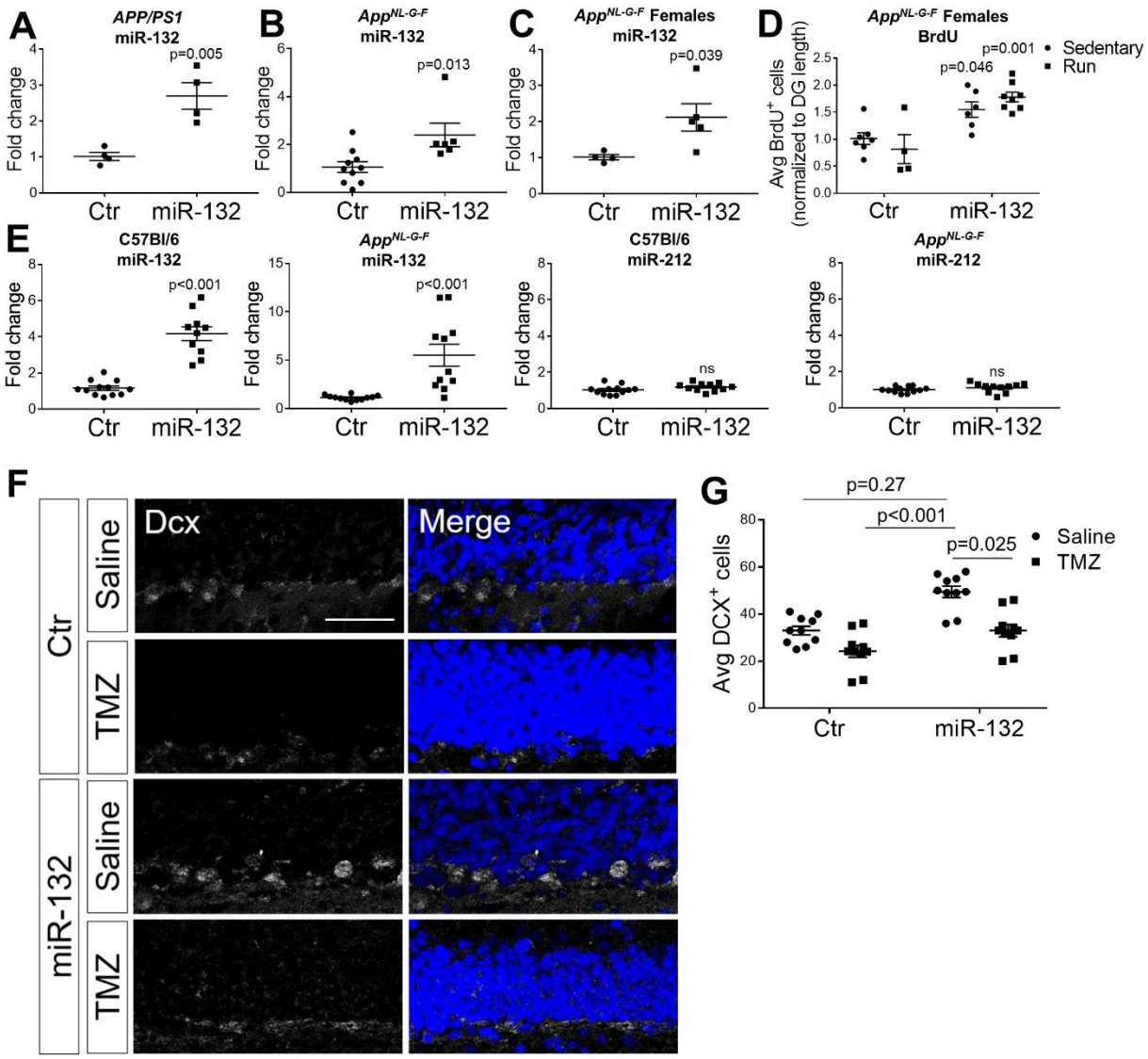

Figure S5. Related to Figures 5 and 8. A, B. Semi-quantitative real-time PCR of miR-132 levels in the dentate gyrus of control- or miR-132-injected 9-month-old *APP/PS1* (A) and *App*$^{NL-G-F}$ (B) mice prior to running. N=4-10 mice per group. C. Semi-quantitative real-time PCR of miR-132 levels in the dentate gyrus of control- or miR-132-injected *App*$^{NL-G-F}$ 9-month-old female mice prior to running. N=4-5 mice per group. D. Quantification of BrdU^{+}-cells in the dentate gyrus of control- or miR-132-injected, sedentary or running *App*$^{NL-G-F}$ female mice at 9 months of age. N=4-8 mice per group. E. Semi-quantitative real-time PCR of miR-132 and miR-212 levels in the dentate gyrus of C57Bl/6 and *App*$^{NL-G-F}$ mice that were exposed to behavioral testing upon miR-132 overexpression. F. Dcx immunolabeling in the dentate gyrus of saline or TMZ-, Ctr- or miR-132-injected *App*$^{NL-G-F}$ mice after passive avoidance test completion. G. Quantification of Dcx^{+}-cells upon saline or TMZ injections in Ctr- or miR-132-

injected *App*$^{NL-G-F}$ mice. N=12 mice per group. Scale bar, 50 µm. Values are presented as mean ± SEM. In (A-C, E), the Student's t-test was applied, while in (D, G), two-way ANOVA with Tukey's *post hoc* test for multiple testing were used.

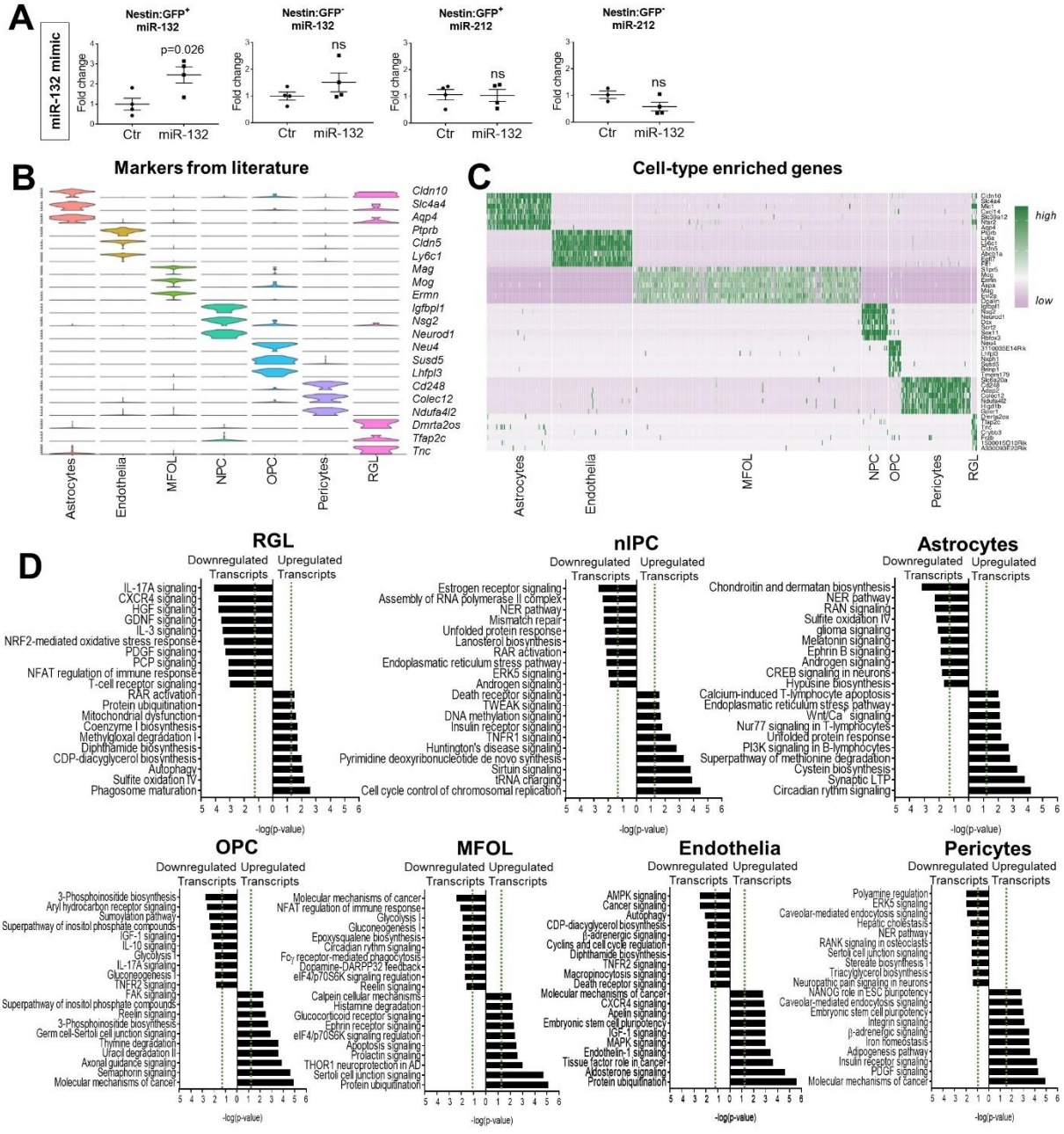

Figure S6. Related to Figure 7. A. Semi-quantitative real-time PCR of miR-132 and miR-212 levels in GFP$^+$ or GFP$^-$ populations sorted from the dentate gyrus of Nestin:GFP mice at 3 months of age upon control- or miR-132-injection. N=4 mice per group; Student's t-test was used. B. Cell type-specific gene

expression of markers derived from previously published datasets. C. Heatmap depicting the expression of the top ten enriched genes per cell type across all identified cells. Each row represents a single cell and each column represents a gene. The expression is normalized by gene. For all significantly upregulated genes per cell cluster, see Table S5. D. Gene ontology enrichment analysis per cluster. Top ten significantly enriched pathways per cluster are indicated for both the 150 most increasing genes (right side of x-axis) and the 150 most decreasing genes (left side of x-axis) upon miR-132 overexpression. The significance values for the canonical pathways were calculated by Fisher's exact test, right-tailed and the threshold for –log(p-value) was set at 1.3 (dashed line).

Supplemental Tables

Table S1. Cases used for immunohistochemical analysis of human dentate gyrus. Related to Figures 1 and S1. Histopathological and clinical scores were determined as previously published and recommended (Rijal Upadhaya et al., 2014). F, female; M, male; Age in years; PMI, postmortem interval (in hours); Aβ-MTL (medial temporal lobe) phase (Thal et al., 2000); Braak-NFT (neurofibrillary tangle) stage (Braak et al., 2006); CERAD (Consortium to Establish a Registry for Alzheimer's Disease)-plaque score for neuritic plaque density (Mirra et al., 1991); NIA-AA (National Institute on Aging–Alzheimer's Association) degree of Alzheimer's pathology (Hyman et al., 2012); CDR (Clinical Dementia Rating) (Morris, 1993); N.A., not available.

Table S2. Antibodies used in the study.

Name	Host	Dilution	Supplier	Catalog number
Anti-BrdU	Rat	1:100	Abcam	ab6326
Anti-GFP	Chicken	1:500	Abcam	ab13970
Anti-Ki-67	Rabbit	1:500	Genetex	GTX16667

Anti-DCX	Rabbit	1:250	Abcam	ab18723
Anti-TUBB3	Mouse	1:200	Biolegend	801202
Anti-GFAP	Rabbit	1:500	DAKO	IS524
Anti-PCNA	Mouse	1:200	DAKO	M0879
Anti-IBA1	Rabbit	1:500	WAKO	019-19741
Anti-NESTIN	Mouse	1:200	R&D Systems	MAB1259
Anti-SOX2	Goat	1:200	Santa Cruz	sc-365823
Anti-Cleaved caspase-3	Rabbit	1:400	Cell Signaling	9661
Anti-VGlUT1	Guinea pig	1:1000	Millipore	AB5905
Anti-PSD95	Mouse	1:200	Thermo Scientific	7E3-1B8
Anti-mCHERRY	Rabbit	1:500	Clontech	632496
Anti-mCHERRY	Goat	1:200	LifeSpan	LS-C204207

Table S3. Primers used in the study.

Primer (microRNAs)	**Target sequence**
mmu-miR-132-3p	UAACAGUCUACAGCCAUGGUCG
mmu-miR-212-3p	UAACAGUCUCCAGUCACGGCCA
mmu-miR-124	UAAGGCACGCGGUGAAUGCC
Primer (messenger RNAs)	**Sequence (5' - 3')**
TUBB3 Forward (Homo sapiens)	CCTCCGTGTAGTGACCCTT
TUBB3 Reverse (Homo sapiens)	GGCCTTTGGACATCTCTTCAG
MKI67 Forward (Homo sapiens)	GAGGTGTGCAGAAAATCCAAA
MKI67 Reverse (Homo sapiens)	CTGTCCCTATGACTTCTGGTTGT
GAPDH Forward (Homo sapiens)	TCAAGAAGGTGGTGAAGCAGG

GAPDH Reverse (Homo sapiens)	ACCAGGAAATGAGCTTGACAAA
18S Forward (Homo sapiens)	TTCGAGGCCCTGTAATTGGA
18S Reverse (Homo sapiens)	GCA GCAACTTAATATACGCTAT
DOCK1 Forward (Homo sapiens)	CTGGCCTTGTTTGTGAACCT
DOCK1 Reverse (Homo sapiens)	TCTTTGCTTCCGAGGTCAGT
EPHB3 Forward (Homo sapiens)	GCTGTGATGACAACGTGGAG
EPHB3 Reverse (Homo sapiens)	TAGTGTGGGCACTTCAGACG
BTG2 Forward (Homo sapiens)	AGGAGGCACTCACAGAGCAC
BTG2 Reverse (Homo sapiens)	CGGTAGGACACCTCATAGGG
CAMK1 Forward (Homo sapiens)	CAAAGATTTCATCCGGCACT
CAMK1 Reverse (Homo sapiens)	TTGAAGGCTTGCTTCCACTT
RAC1 Forward (Homo sapiens)	TTTGAAAATGTCCGTGCAAA
RAC1 Reverse (Homo sapiens)	TCGCTTCGTCAAACACTGTC
JUN Forward (Homo sapiens)	CCCCAAGATCCTGAAACAGA
JUN Reverse (Homo sapiens)	CCGTTGCTGGACTGGATTAT
CD320 Forward (Homo sapiens)	GGCTGTGGAACCAATGAGAT
CD320 Reverse (Homo sapiens)	CAGAGGAGGATGTGGCATTC
SESN3 Forward (Homo sapiens)	CCCTTGACAAGAGGACCAAG
SESN3 Reverse (Homo sapiens)	CCATGCGCAACATGTAAAAC
MSN Forward (Homo sapiens)	ATCACTCAGCGCCTGTTCTT
MSN Reverse (Homo sapiens)	CCCACTGGTCCTTGTTGAGT
TMCC3 Forward (Homo sapiens)	CATGAGACAGCCAACCTGAA
TMCC3 Reverse (Homo sapiens)	AGAATGTGGCAGCGACTCTT
TNIK Forward (Homo sapiens)	AAATCTTACGGGGGCTGAGT
TNIK Reverse (Homo sapiens)	TGCCATCCAGTAGGGAGTTC

PDHX Forward (Homo sapiens)	CCAAAGACGTAGGTCCTCCA
PDHX Reverse (Homo sapiens)	TGGCTAGCATCCAGTGAGTG
DENR Forward (Homo sapiens)	CCAAGGAACAGTGCCAAGTT
DENR Reverse (Homo sapiens)	GACCCCTTCCACCTCTCTTC
FOS Forward (Homo sapiens)	AGAATCCGAAGGGAAAGGAA
FOS Reverse (Homo sapiens)	CTTCTCCTTCAGCAGGTTGG
UBR5 Forward (Homo sapiens)	ATTGCTGTGCCCTTTACACC
UBR5 Reverse (Homo sapiens)	TGAAAATGCAACTGCTCCAG
COA3 Forward (Homo sapiens)	GACTCGGGAGAAGCTGACAC
COA3 Reverse (Homo sapiens)	CTTTGGCCTCGTCTTCTAGC
ZMYM5 Forward (Homo sapiens)	TATCGAATGGGGACTTCCTG
ZMYM5 Reverse (Homo sapiens)	CCCCTGGCTGTTTCTGATTA
MGA Forward (Homo sapiens)	CTCTCCAAATGTCCCTGGAA
MGA Reverse (Homo sapiens)	TGTTGTCCCATCAACTGCAT
CORO7 Forward (Homo sapiens)	CTGGTGTACTGGGCATTGTG
CORO7 Reverse (Homo sapiens)	GCAGTCGCCAGAGTTTTACC
GSK3B Forward (Homo sapiens)	TTCCTTTGGAATCTGCCATC
GSK3B Reverse (Homo sapiens)	ACAGCTCAGCCAACACACAG
EFHD1 Forward (Homo sapiens)	GGCAAAGCTTTCTGAGATCG
EFHD1 Reverse (Homo sapiens)	GTTGGCCTTGAGTTTCTGGA
ZHX3 Forward (Homo sapiens)	CTGAGCAGCATTCCAACGTA
ZHX3 Reverse (Homo sapiens)	AACCGTAATTGTGGGCTGAG
CDC40 Forward (Homo sapiens)	CCTCAGTGCAGCCTATGACA
CDC40 Reverse (Homo sapiens)	GGTGTTGACAGCTCCCAAAT
PPP2R5C Forward (Homo sapiens)	AGCCAATCCCCAGTACACAG

PPP2R5C Reverse (Homo sapiens)	ACGGTCCTTCTTCGGATCTT
AAK1 Forward (Homo sapiens)	GCACCAGAAATGGTCAACCT
AAK1 Reverse (Homo sapiens)	GGCAGTGCATGTCTTGAGAA
PSME4 Forward (Homo sapiens)	TTCAGCCACAGCTGAATTTG
PSME4 Reverse (Homo sapiens)	ACCATGCGACCTGCTACTCT
SLC1A4 Forward (Homo sapiens)	AGCTCAACGCAGGACAGATT
SLC1A4 Reverse (Homo sapiens)	GCTTCCACTTTCACCTCAGC
UTRN Forward (Homo sapiens)	AGTCACCATAGACGCCATCC
UTRN Reverse (Homo sapiens)	GTCCTCAGCAGAAAGCAACC
FAM168A Forward (Homo sapiens)	TTACCCCACAGCCTATCCAG
FAM168A Reverse (Homo sapiens)	AGTGCCACAGGAAGACGAGT
CLDN10 Forward (Homo sapiens)	GATCATCGCCTTCATGGTCT
CLDN10 Reverse (Homo sapiens)	GCTGACAGCAGCGATCATAA
CHMP1A Forward (Homo sapiens)	AAGAAGGCGGAGAAGGACTC
CHMP1A Reverse (Homo sapiens)	GGTCACCCCCTTCATAGTCA
GCSH Forward (Homo sapiens)	GAAGCGTTGGGAGATGTTGT
GCSH Reverse (Homo sapiens)	CCTGGATTTTCTGCAAGAGC
RASA1 Forward (Homo sapiens)	AGCGAAAAACGAGCTACCAA
RASA1 Reverse (Homo sapiens)	CGAAGGCGTTTATTGGATGT
EXOC6B Forward (Homo sapiens)	GAACTGTGGGAAATGGCACT
EXOC6B Reverse (Homo sapiens)	ACCTGCCCACTTCTTTAGCA
ORAI3 Forward (Homo sapiens)	GAAGCTGTGAGCAACATCCA
ORAI3 Reverse (Homo sapiens)	AACTTGACCCAACCAACCAG
HDAC3 Forward (Homo sapiens)	TGGCTTCTGCTATGTCAACG
HDAC3 Reverse (Homo sapiens)	GTTGATAACCGGCTGGAAAA

USE1 Forward (Homo sapiens)	GCAGCTGAGCTAGACCTCGT
USE1 Reverse (Homo sapiens)	GTCCGCCATTTTCAGTGAGT
SLC25A12 Forward (Homo sapiens)	CTGAGGGGGCCTTACCTTAC
SLC25A12 Reverse (Homo sapiens)	CATTCGGGTCTTCACCAGAT
SLC35B4 Forward (Homo sapiens)	ATTCCAGGCATTTGTGTGGT
SLC35B4 Reverse (Homo sapiens)	GATGGATTCCAGGCATTTGT
PLXNB2 Forward (Homo sapiens)	TCCAGCTCCTCCTTAGACGA
PLXNB2 Reverse (Homo sapiens)	AGGTTCTTGCCCTGGAAGTT
ADAMTS1 Forward (Homo sapiens)	ACGAGTGCGCTACAGATCCT
ADAMTS1 Reverse (Homo sapiens)	TCCTTGCACACAGACAGAGG
ATP6V0A1 Forward (Homo sapiens)	GTCACCGACCTTGACTCCAT
ATP6V0A1 Reverse (Homo sapiens)	AATGCCATGACCGAAGTCTC
SIPA1L3 Forward (Homo sapiens)	ACCCCTGCACTGATAACGTC
SIPA1L3 Reverse (Homo sapiens)	GGTGTGGAACTTGTCGGACT
CBFA2T2 Forward (Homo sapiens)	CACGAACACCTTCTGCTCAA
CBFA2T2 Reverse (Homo sapiens)	GTGGAGGGGTAGGATGGAAT
KAT7 Forward (Homo sapiens)	GAAATGCGCCTTCTTCTGAG
KAT7 Reverse (Homo sapiens)	TGTGCTCTCACCTTGCATTC
CIAO1 Forward (Homo sapiens)	CCCACACACAGGATGTCAAG
CIAO1 Reverse (Homo sapiens)	GACGCCAGATACGCACAGTA
GAPVD1 Forward (Homo sapiens)	TGTTAGGCAGTTTGCTGTGC
GAPVD1 Reverse (Homo sapiens)	CCCAGTCCAGAACAGCTCTC
ABCF1 Forward (Homo sapiens)	GACCACACTCCTCAAGCACA
ABCF1 Reverse (Homo sapiens)	CCGCAATTCCTCATACACCT
CRKL Forward (Homo sapiens)	ATCTGTCTCAGCACCCAACC

CRKL Reverse (Homo sapiens)	GGCACTCCACCACTGTTCTT
DIP2A Forward (Homo sapiens)	CCTGTGATGTTCATGGTTGC
DIP2A Reverse (Homo sapiens)	TCTGACAAGCGTCTGTGGTC
MDM4 Forward (Homo sapiens)	TGGGTACTGCCATTGTTTCA
MDM4 Reverse (Homo sapiens)	CACTGCCACTCATCCTCAGA
ASCC2 Forward (Homo sapiens)	TCAGGGCTTCATCGAAGAGT
ASCC2 Reverse (Homo sapiens)	CACCGATGGGTCTTTAGCAT
Stx1A Forward (Mus musculus)	AGCACAACATACCCTGTGG
Stx1A Reverse (Mus musculus)	GGTCTTCCAGTTACCCGACA
Syp Forward (Mus musculus)	TGCCAACAAGACGGAG
Syp Reverse (Mus musculus)	GGCGGATGAGCTAACT
Pax6 Forward (Mus musculus)	AACAACCTGCCTATGCAACC
Pax6 Reverse (Mus musculus)	ACTTGGACGGGAACTGACAC
Mki67 Forward (Mus musculus)	GTCCCTCAAAAGCAGACGAG
Mki67 Reverse (Mus musculus)	GCTGCTGCTTCTCCTTCACT
Dcx Forward (Mus musculus)	TCCCCAACACCTCAAAAGAC
Dcx Reverse (Mus musculus)	ATGGAATCGCCAAGTGAATC
Actb Forward (Mus musculus)	TCCTCCCTGGAGAAGAGCTA
Actb Reverse (Mus musculus)	GCAATGATCTTGATCTTC
Gapdh Forward (Mus musculus)	TTGATGGCAACAATCTCCAC
Gapdh Reverse (Mus musculus)	CGTCCCGTAGACAAAATGGT

Table S4. Information on serum samples used in the '*in vitro* parabiosis' assay. Related to Figures 4 and S4. Blood samples were drawn and biochemically characterized as previously described

(Johansson et al., 2013). n, sample size; Age in years; SD, standard deviation; T-tau, total tau; P-tau, tau phosphorylated at threonine 181.

Table S5. Cell-type mapping. Related to Figures 7 and S6. Seurat's "AddModuleScore" function, with default parameters, was used to calculate gene set scores of cell type-specific markers extracted from previous studies (LiteratureMarkers). Boxplots of these scores were used to assign each cluster to a cell type (summary data provided under ModuleScore). Cluster markers were determined by differential expression analysis of each cluster versus all other clusters combined (ClusterMarkers). Qu, quartile; RGL, radial glia-like neural stem cells; NPC, neuronal intermediate progenitor cells; OPC, oligodendrocyte precursor cells; MFOL, myelin-forming oligodendrocytes; p_val, p-value; avg_logFC, average of log fold change; p_val_adj, adjusted p-value using the Bonferroni correction.

Table S6. Differential expression analysis in single Nestin:GFP^{+}-niche cells. Related to Figures 7 and S6. Differential expression analysis was performed between miR-132-overexpression and control group in RGL (radial glia-like neural stem cells), NPC (neuronal intermediate progenitor cells), astrocytes, OPC (oligodendrocyte precursor cells), MFOL (myelin-forming oligodendrocytes), endothelial cells and pericytes. p_val, p-value; avg_logFC, average of log fold change; pct1, percentage of cells in first group (miR-132 overexpression group); pct2, percentage of cells in second group (control group); p_val_adj, adjusted p-value using the Bonferroni correction; DE, differential expression.

Click here to access/download

Supplemental Videos and Spreadsheets

Supplementary video S1

Click here to access/download

Supplemental Videos and Spreadsheets

Supplementary video S2

Click here to access/download

Supplemental Videos and Spreadsheets

Table S1.xlsx

Click here to access/download

Supplemental Videos and Spreadsheets

Table S4.xlsx

Click here to access/download

Supplemental Videos and Spreadsheets

Table S5.xlsx

Click here to access/download

Supplemental Videos and Spreadsheets

Table S6.xlsx